6

SUMMARY, CONCLUSIONS AND FUTURE WORK

A proper characterization of extensive ice masses, with high spatial and temporal resolution, is an important requirement in the determination of their impact on the Earth's climate. The present dissertation has evaluated the use of reflected GNSS signals towards remote sensing of the cryosphere. Despite being tested for a wide variety of applications, this technique is rather novel and represents a low cost source of opportunity for the monitorization of ice masses in Polar environments, a task specially challenging to be done in situ due to extreme weather conditions.

The research described along this dissertation could be classified in two main blocks, each of them dedicated to analysis of a different type of ice extensions: thin –hundreds of centimeters– sea ice covers; and thick –hundreds of meters– dry snow accumulations (mostly located in Antarctica and interior of Greenland). In both cases, theoretical studies and models have been developed, and their applicability has been supported by the results obtained from in situ experimental campaigns. Dedicated comments for each part are given afterwards.

Overall, the work presented here constitutes a first step toward ancillary applications that might be relevant to a possible future PARIS space-based mission (Martín-Neira et al., 2011). Such a mission, currently at the feasibility assessment level, will possibly follow a near-polar orbit, which would densely sample the vast Arctic and Antarctic areas. As a first recommendation for future work, further investigation to get a more comprehensive extrapolation of these results to a spaceborne scenario would be required.

6.1 REMOTE SENSING OF SEA ICE

One of the most significant parameters used for sea ice classification is its thickness, which can be estimated with accurate altimetric measurement of the freeboard level. In addition, permittivity and roughness retrievals might play a key role towards the same general purpose of characterizing sea ice extensions. Different GNSS-R observables have been analyzed to estimate these parameters during an experimental field campaign in Disko Bay, Greenland, from November 2008 until May 2009. The main difficulties faced during the analysis of the data have been related to (1) geometry, since the low elevation range available provoked overlapping between direct and reflected signals and failure of the standard known models; (2) technical aspects, mainly due to problems with the RHCP-R antenna's connector and strong presence of near-by multipath; and (3) lack of more detailed in-situ data with similar spatial resolution as the GNSS-R measurements.

Altimetric estimations of the sea surface level have been made based on the use of two different observables: code- and phase-delay. While the difficulties previously mentioned hinder the proper altimetric retrieval under the first approach, the second methodology achieves better performances. The time evolution of the phase-delay retrieved heights matches with an Arctic tide model. In addition, the results obtained with reflected GPS signals at different polarizations are consistent and their combination enables a continuous height retrieval for the whole campaign's period. While the mean formal precision of the single-track (~ 1 km) estimates is ~ 3 cm, the 1-day averaged measurements show a RMS standard deviation of 15.4 cm. The slow evolution of the height retrievals (once corrected with the tide model) follows the variation of the ice surface temperature provided by MODIS, which is a key parameter in the rate of growth of sea ice. In absence of a proper ground truth, the range of the available altimetric measurements from ICESat GLAS obtained during the last years in the experimental site has been compared with the GNSS-R estimates, and it agrees with our estimations. However, the lack of more detailed ice information such as density and thickness (for comparison) hindered the performance of a proper retrieval of this last parameter from the altimetric results. In addition, the penetration of the L-band signal through sea ice should be also determined, which requires accurate determination of its permittivity.

The retrieval of sea surface roughness has also followed two different approaches. The first one explores how the scattering redistributes the power along the GNSS-R waveform by obtaining a secondary intermediate observable, called scatterometric delay, and then inferring from it a *MSS* estimation by means of a standard KGO-based electromagnetic model. Despite that the general variation of the results obtained show a realistic pattern, with peaks during high winds (provided by QuikSCAT) in open waters and minimums during presence of smoother sea ice, further empirical corrections are needed to reach the expected range of *MSS* values according to previous experiments. We consider that the reasons are the limitations of the standard electromagnetic models to reproduce GNSS-R waveforms at such low angles of elevation, together with the contamination of direct signal into the reflected waveforms. Compared against the ice form information provided by DMI's ice charts, the resultant *MSS* retrievals reach their lowest values when compact ice floes are present, forming then a smooth sea surface, while they significantly increase with presence of just ice growlers, where the roughness conditions are still imposed by the wind/water interaction, and for consolidated fast ice, which provides a rougher reflecting surface due the continuous ice cracking forced by the ocean tides. The second method under analysis makes use of the variability of the interferometric phase, which contains altimetric information, to perform an estimation of the RMS of the surface height level (RMS_H), a parameter often employed to characterize surface roughness. However, the results obtained show a strong dependency with the signal's power level, which is also related to the dielectric characteristics of the reflecting surface, thus being unable to achieve the proper separability between permittivity and roughness.

As in the other cases, two methodologies have been tested to obtain reflectivity estimations linked to the dielectric properties (permittivity) of the ocean surface. Both of them exploit polarimetric observables, that is, combining RHCP and LHCP reflected signals to determine the presence and evolution of sea ice by means of the Fresnel reflection components. The first approach consists of measuring the polarimetric ratio of the peak power waveforms with opposed polarizations. The evolution of these results during presence of sea ice shows good agreement with ice concentration measurements obtained with visual inspection from a local Arctic weather station, as well as with the same information provided by DMI's ice charts. The sensitivity of this method depends on the elevation angle. Being the slant geometries of this experimental scenario closer to the Brewster angle, they are more sensitive to variations in permittivity. The second method takes the phase difference of these waveforms with opposed polarizations (POPI). This method should be independent of the elevation angle. Due to limitations in the receiver's internal configuration, the phase values were affected by an undetermined offset. For this reason, the analysis has to be limited to comparisons against the polarimetric ratio along the same ground track. There is correspondence between the evolution of both retrievals, specially during their most significant variations (presumably due to water/ice transitions). However, decorrelated fluctuation patterns are found when general high values are reached (due to presence of sea ice). Motivated by the possibility of interaction between reflections from sea ice and sea water (due to penetration of the incident signal through ice), a simple interferometric approach has been tested without success, so further research is needed to maximize the outcome of the POPI observable.

The main novelty introduced in the GNSS-R remote sensing of sea ice have been the use of polarimetric measurements, both phase and power observables. Next step should be a series of aircraft experiments, choosing a ground-track with a variety of sea ice conditions; repeating the ground-track several times, at different altitudes; and with ancillary instrumentation to measure and contrast the same parameters that GNSS-R might be sensitive to (e.g. roughness, permittivity, altimetry). These instruments should be either on-board or ground-based as in-situ proves. The ancillary ground truth should be also used to improve the modeling of the signal: to introduce a realistic probability density functions for different sea-ice (we have been using Gaussian distributions with typical standard deviations as in the roughness of open waters); and to incorporate multi-layer and even volumetric scattering models (sea-ice with snow coverage, with multi-layer salinity gradients or snow volumetric scattering). Such an experiment should help compiling the information required to extrapolate the results to space-based scenarios: geometries closer to nadir, and gauging the effects of the receiver's altitude on, not only SNR, but also parameters related to coherence of the reflected signals.

6.2 REMOTE SENSING OF DRY SNOW

The interference fringes found in GNSS-R observables collected during an experimental field campaign at Dome Concordia, Antarctica, December 2009, cannot be explained by near-by multipath or external reflecting elements. In addition, the patterns show strong temporal repeatability. All indications point to reflections off internal layers of the snow as sources of these interference fringes. A simple model, Multiple-Ray Single-Reflection (MRSR), of L-band scattering and propagation through sub-surface layers of snow has been developed, and its qualitative agreement with the data is shown. The main conclusion is that the L-band GNSS signals penetrate into the snow, are reflected by some of its layers, and the reflected components interfere with each other and with the direct radio-link to generate the observed beating patterns. The depth of penetration is estimated to be down to 200-300 meters, and a few of the layers are more reflecting than the rest.

These foremost reflecting layers are identified by means of a radio-holographic technique, applied independently on each lag of the GNSS waveform, thus building a new observables, that we have called lag-hologram. Further delayed lags of the waveform contain information about signal being more delayed with respect to the reference –direct– signal. Therefore, the complete lag-space must be inspected rather than just the peak of the signal, in order to obtain information from reflections occurring at deeper layers. While the lag-hologram identifies bright frequency stripes, the MRSR can also be used to link these frequencies into the depths of the reflecting layers that induced them. It has been shown that this translation is rather independent of inaccuracies in the a-priori snow density profile used by the model. The sole knowledge of the most reflecting layers might be of interest to complement L-band radiometric experiments, such as the spaceborne SMOS and Aquarius missions. An example has been shown when comparing brightness temperature anomalies detected by a L-band radiometer placed in the same location with an adapted version of the MRSR. The fluctuation pattern found in the radiometric measurements has good agreement with the modeled signal coming from the Sun and reflected off the snow layers.

The attempts to invert real data into a complete layered permittivity profile by using a linearized approach have not been fruitful. In general, the solution strongly relates to the a-priori profile, even when loose covariances are given. The impression is that the real data lag-holograms present a set of high negative frequency bands in the central lags, which are not predicted by the model. It is unclear whether the model does not predict them or it would, but these bands rest masked because it overestimates the surface reflection.

This study is pioneer in GNSS-R remote sensing of deep dry snow layers based on multiple reflections. Despite the high temporal repeatability of the interferometric features found in the real data, the geographic consistency is rather low. Perhaps we are sensing inhomogeneities in the snow, but this has not been proven. Several other reasons that might explain this performance are contained in the validity of the model's assumptions: locally horizontal snow layers, single layer-reflections and an homogeneous density profile for the entire area, $\sim$500 meter wide. All these assumptions should be carefully revised, and improvements in the model could be made to attempt more complete retrievals of the snow sub-surface contents. For instance, estimates of the snow density or permittivity could be refined with the appropriate forward model; or tomographic approaches implemented to solve for the 3-D structures, including tilted layers and spatial inhomogeneities. Despite this limitation, the detection of the reflective layers can still be useful. As an example, in Hawley et al. (2006), the delays of radar measurements are not used to estimate the snow density, but combined with a given density profile to estimate the snow accumulation rates. A similar application can be envisaged for GNSS-R.

A

GLOSSARY OF TERMS

A.1 LIST OF ACRONYMS

2SCM	Two-Scale Composite Model
ALI	Advanced Land Imager
ALOS	Advanced Land Observing Satellite
AMSR-E	Advanced Microwave Scanning Radiometer for EOS
AMSU	Advanced Microwave Sounding Unit
AOTIM	Arctic Ocean Tidal Inverse Model
ASAR	Advanced Synthetic Aperture Radar
ASCAT	Advanced Scatterometer
AVHRR	Advanced Very High Resolution Radiometer
AWS	Automatic Weather Station
BOC	Binary Offset Carrier
BPSK	Binary Phase Shift Keying
C/A-(code)	Coarse/Acquisition (GPS code)
CDMA	Code Division Multiple Access
CEOS	Committee on Earth Observation Satellites
CHAMP	Challenging Mini-satellite Payload
CoSMOS-OS	Campaign on SMOS - Ocean Salinity
CSIC	Consejo Superior de Investigaciones Científicas / Spanish Research Council
DB	Database
DDM	Delay Doppler Map
DMC	Disaster Monitoring Constellation
DMI	Danmarks Meteorologiske Institut / Danish Meteorological Institute
DMSP	Defense Meteorological Satellite Program
DoD	Department of Defense
DoY	Day of Year
ECMWF	European Centre for Medium-Range Weather Forecasts
ECV	Essential Climate Variables
EGM96	Earth Gravitational Model 1996
Envisat	Environmental Satellite
EOS	Earth Observing System
ERS	European Remote Sensing satellite

ESA	European Space Agency
ETM+	Enhanced Thematic Mapper Plus
FDMA	Frequency Division Multiple Access
FFT	Fast Fourier Transform
GCOS	Global Climate Observing System
GEO	Geostationary Orbit
GFZ	GeoForschungsZentrum / German Research Centre for Geosciences
GLAS	Geoscience Laser Altimeter System
GLONASS	Global'naya Navigatsionnaya Sputnikovaya Sistema / Global Navigation Satellite System
GMES	Global Monitoring for Environment and Security
GMF	Global Mapping Function
GNSS	Global Navigation Satellite Systems
GNSS-R	Global Navigation Satellite Systems - Reflectometry
GOLD-RTR	GPS Open Loop Real Time Receiver
GORS	GNSS Occultation, Reflectometry and Scatterometry space receiver
GPS	Global Positioning System
GPS-R	Global Positioning System - Reflectometry
GPS-SIDS	GPS - Sea Ice Dry Snow
GTOS	Global Terrestrial Observing System
HH	Horizontal-input to Horizontal-output polarization
HTTP	Hypertext Transfer Protocol
HV	Horizontal-input to Vertical-output polarization
ICE	Institut de Ciències de l'Espai / Institute of Space Sciences
ICESat	Ice, Cloud, and land Elevation Satellite
IEEC	Institut d'Estudis Espacials de Catalunya / Institute for Space Studies of Catalonia
IFAC	Nello Carrara Istituto di Fisica Applicata / Institute of Applied Physics
IFREMER	Institut Français de Recherche pour l'Exploitation de la Mer / French Research Institute for Exploitation of the Sea
IGS	International GNSS Service
IGSO	Inclined Geosynchronous Orbit
INT	Integrated Data (non-coherently at 1 sec)
IOV	In-Orbit Validation (space vehicle)
IP	Internet Protocol
IPCC	Intergovernmental Panel on Climate Change
I&Q	In-phase and Quadrature
KGO	Kirchhoff approximation under Geometric Optics
KM	Kirchhoff Method
LAN	Local Area Network
LEO	Low Earth Orbit

LGGE	Laboratoire de Glaciologie et Geophysique de l'Environnement / Laboratory of Glaciology and Geophysics of the Environment at Grenoble
LHCP	Left Hand Circular Polarization
LIDAR	Light Detection And Ranging
LL	LHCP-input to LHCP-output polarization
LNA	Low Noise Amplifier
LR	LHCP-input to RHCP-output polarization
M-(code)	Military (GPS code)
MEO	Medium Earth Orbit
MetOp	Operational Meteorology
MIRAS	Microwave Imaging Radiometer using Aperture Synthesis
MODIS	Moderate-resolution Imaging Spectroradiometer
MRSR	Multiple-Ray Single-Reflection model
MSS	Mean Square Slope
MySQL	My Structured Query Language
NASA	National Aeronautics and Space Administration
NWPM	Numerical Weather Prediction Model
NW-SE	North-West to South-East
PALSAR	Phased Array type L-band Synthetic Aperture Radar
PARIS	Passive Reflectometry and Interferometry System
PDF	Portable Document Format
POES	Polar Operational Environmental Satellite
POPI	POlarimetric Phase Interferometry
PRN	Pseudorandom Noise (sequence)
P(Y)-(code)	Encrypted Precise (GPS code)
QuikSCAT	Quick Scatterometer
RA	Radar Altimeter
RAW	Raw Sampling Data (complex phasors at 1 msec)
RF	Radio Frequency
RHCP	Right Hand Circular Polarization
RL	RHCP-input to LHCP-output polarization
RMS	Root Mean Square
RR	RHCP-input to RHCP-output polarization
RSS	Residual Sum of Squares
Rx	Receiver
SAR	Synthetic Aperture Radar
SIRAL	SAR/Interferometric Radar Altimeter
SMOS	Soil Moisture Ocean Salinity satellite
SNR	Signal to Noise Ratio
SPM	Small Perturbation Method
SSA	Small Slope Approximation
SSH	Secure SHell
SSM/I	Special Sensor Microwave/Imager
SSMI/S	Special Sensor Microwave Imager/Sounder
SVN	Apache Subversion

TanDEM-X	TerraSAR-X add-on for Digital Elevation Measurement
TU	Terminal Unit
Tx	Transmitter
TZD	Total Zenith Delay
UAV	Unmanned Aerial Vehicle
UDP	User Datagram Protocol
UE	User End
UHF	Ultra High Frequency
UK	United Kingdom
UMTS	Universal Mobile Telecommunications System
UTC	Coordinated Universal Time
VH	Vertical-input to Horizontal-output polarization
VLBI	Very-Long-Baseline Interferometry
VV	Vertical-input to Vertical-output polarization
WAV	Woodward Ambiguity Function
WGS84	World Geodetic System 1984
WIST	Warehouse Inventory Search Tool
WMO	World Meteorological Organization
WS	Wind Scatterometer
ZHD	Zenith Hydrostatic Delay
ZWD	Zenith Wet Delay

A.2 LIST OF SYMBOLS

A_0	Illuminated area.
A_{eff}	Effective area of receiver antenna.
A_M	Multipath's amplitude.
A_{res}	Amplitude of the sawtooth wave that models the impact of ΔH in the variation of $\Delta\phi_I$.
$\overline{A_i S}$	Distance between point A_i (wavefront reaching the surface for internal reflection at *i*-layer) and Specular reflection point in the MRSR model for dry snow remote sensing.
$\vec{b}$ / $[b]$	Vector/array of the inter-antenna baseline distance.
B	Receiver's bandwidth.
$B_{C/A} = 2.046$ MHz	Bandwidth of the GPS C/A signal.
$c = 299792458$ m/s	Speed of light in the free space.
$C(t)$	Ranging code.
$C_{C/A}(t)$	C/A-code sequence.
$C_{P(Y)}(t)$	P(Y)-code sequence.
$C_I \equiv E_r \cdot E_d^*$	Interferometric coherence-field.
$C_{pol} = E_r^{RHCP} \cdot E_r^{LHCP*}$	Polarimetric field.
$C_{\mathcal{W}}$	Data covariances for lag-hologram total inversion.
C_ρ	Model covariances for lag-hologram total inversion.
d_i	One-way physical distance traveled inside the *i*-layer in the MRSR model for dry snow remote sensing.
$D(t)$	Navigation data message.
D_{hz}	Zenith hydrostatic delay.
D_{wz}	Zenith wet delay.
$D_z = D_{hz} + D_{wz}$	Total Zenith Delay (TZD).
D_i	Horizontal extent of the propagation inside the *i*-layer in the MRSR model for dry snow remote sensing.
$e = 2.7182818$	Euler's number.
$\vec{e}$ / $[e]$	Unit vector/array that defines the arrival direction of the signal reflected at the specular point.
E_0	Maximum amplitude of the incident electric field.
E_{inc}	Incident electric field towards the reflecting target.
E_d	Direct field.
E_r	Reflected field.

E_r^{pq}	Reflected electric field in the pq polarization state, i.e. p as input polarization and q as output polarization. If p and q are the same polarization, the term *co* (co-polar) is employed; on the other hand, when p and q are opposite polarizations, the term *cross* (cross-polar) is used. In the case of GPS signals, transmitted at RHCP polarization, $E_r^{co} = E_r^{RHCP}$ and $E_r^{co} = E_r^{LHCP}$.
$\vec{E}^s_{pq}$	Scattered electric field in the pq polarization state, i.e. p as input polarization and q as output polarization.
E1	GNSS Frequency band between 1587.0 and 1591.0 MHz employed by Galileo and BeiDou-2/Compass. Some references define E1 to the joint E2-L1-E1 given here.
E2	GNSS Frequency band between 1559.0 and 1563.0 MHz employed by Galileo and BeiDou-2/Compass.
E5A	GNSS Frequency band between 1164.0 and 1189.0 MHz employed by Galileo and BeiDou-2/Compass, overlapping with L5.
E5B	GNSS Frequency band between 1189.0 and 1214.0 MHz employed by Galileo and BeiDou-2/Compass, overlapping with G3.
E6	GNSS Frequency band between 1260.0 and 1300.0 MHz employed by Galileo and BeiDou-2/Compass.
$f(t)$	Carrier RF sinusoidal signal.
f_I	Interferometric frequency.
f_I^{surf}	Interferometric frequency corresponding to the surface snow level.
$f_{L1} = 1575.42$ MHz	GPS L1 carrier frequency.
$f_{L2} = 1227.60$ MHz	GPS L2 carrier frequency.
$f_{L5} = 1176.45$ MHz	GPS L5 carrier frequency.
f_M	Multipath frequency relative to the main signal.
f_L	Linearized function for Lag-Hologram total inversion.
F_{eq}	Equivalent noise figure of the RF front-end.
F_L	Matrix of the partial derivatives of f_L, numerically computed around the a-priori profile $\widehat{\rho_s}$.
F_{LNA}	LNA noise figure.
$\mathcal{F}\{\}$	Fast Fourier Transform.
G_a	Antenna gain.
G_{LNA}	LNA gain.
G_r	Receiver antenna gain (directivity).
G_t	Transmitter antenna gain (directivity).
G1	GNSS Frequency band between 1593.0 and 1610.0 MHz employed by GLONASS.

G2	GNSS Frequency band between 1237.0 and 1254.0 MHz employed by GLONASS, overlapping with L2.
G3	GNSS Frequency band between 1189.0 and 1214.0 MHz employed by GLONASS, overlapping with E5B.
$h_{scale} = 7160$ m	Scale height of the troposphere assumed during Greenland-dataset processing.
H_i	Height (vertical width) of the i-layer in the MRSR model for dry snow remote sensing. In the case of $i = 0$ (air layer), H_0 corresponds to the height of the receiver's antenna with respect to the snow surface level.
H_M	Height of the receiver antenna above the multipath-reflector.
H_S^R	Vertical distance between receiver antenna and specular point of reflection.
H_{ellip}^S	Height of the surface with respect to the reference ellipsoid WGS84 (ellipsoidal height).
H_{MAX}	Ellipsoidal height retrieved using code-delay from maximum of the waveform.
H_{DER}	Ellipsoidal height retrieved using code-delay from maximum of the waveform's first derivative.
H_{WGS84}	Height between the reference ellipsoid WGS84 and the sea ice surface level.
H_{sea}	Mean sea level with respect to WGS84.
$i = \sqrt{-1}$	Imaginary unit.
$\mathcal{I}m\{\}$	Imaginary part.
k	Wavenumber.
k_i	Wavenumber across the i-layer in the MRSR model for dry snow remote sensing.
$K = 1.38 \times 10^{-23}$J/K	Boltzmann's constant.
L	Non-modeled losses in the radar equation (e.g. atmospheric loss).
L_c	Attenuation of the cable.
L_{corr}	Transversal correlation length of the reflecting surface.
L1	GNSS Frequency band between 1563.0 and 1587.0 MHz employed by GPS.
L2	GNSS Frequency band between 1215.0 and 1239.6 MHz employed by GPS, overlapping with G2.
L5	GNSS Frequency band between 1164.0 and 1189.0 MHz employed by GPS, overlapping with E5A.

m_v	Volume fraction of liquid water in the snow mixture.
m_{hz}	Hydrostatic mapping function.
m_{wz}	Wet mapping function.
mss	One-dimensional mean square slope.
MSS	Two-dimensional mean square slope (or simply mean square slope).
MSS_0	A-priori mean square slope value for MSS-inversion.
n	Refractive index.
n_i	Refractive index of the i-layer in the MRSR model for dry snow remote sensing.
$\hat{n}_s$	Normal scattered vector.
$\hat{n}_i$	Normal incident vector.
$P_{C/A_{L1}}$	Signal power for GPS signals carrying C/A-code on L1.
$P_{P(Y)_{L1}}$	Signal power for GPS signals carrying P(Y)-code on L1.
$P_{P(Y)_{L2}}$	Signal power for GPS signals carrying P(Y)-code on L2.
P_r	Power sensed by the receiver antenna.
P_t	Power transmitted.
P	Probability Density Function of the surface slopes for a Gaussian isotropic surface spectrum.
$\vec{q} = (q_x, q_y, q_z) \equiv k(\hat{n}_s - \hat{n}_i)$	Scattering vector, perpendicular to the local tangent plane.
$\vec{q}_\perp = (q_x, q_y)$	Components of $\vec{q}$ perpendicular to the incidence plane.
$r_{corr} \equiv \sqrt{x_{corr}^2 + y_{corr}^2}$	Correlation radial distance.
R_{eff}	Effective sampling rate.
R_0	Distance from the point of observation (receiver) to the center of A_0.
R_1	Distance from transmitter to target.
R_2	Distance from target to receiver.
R_d	Electromagnetic path length of the direct signal.
R_r	Electromagnetic path length of the reflected signal.
RMS_ϕ	Root mean square of the complex field's phase ϕ_I.
RMS_H	Contribution in RMS_ϕ from the residual height, related to surface roughness.
$RMS_{fad/coh}$	Contribution in RMS_ϕ from the impact of random phase departures produced by fading and coherence loss.
RMS_{mpath}	Contribution in RMS_ϕ from distortion of the phase due to multipath.
RMS_N	Contribution in RMS_ϕ from instrumental noise.
RMS_{res}	Contribution in RMS_ϕ due to the impact of an error in the height estimation.

$Rot_x(\theta_{BF})$	Rotation matrix around x-axis in the local body-frame.
$Rot_y(\phi_{BF})$	Rotation matrix around y-axis in the local body-frame.
$Rot_z(\psi_{BF})$	Rotation matrix around z-axis in the local body-frame.
$\mathcal{R}e\{\}$	Real part.
$\Re_{pq}$	Fresnel coefficient in the pq polarization state, i.e. p as input polarization and q as output polarization. If p and q are the same polarization, the term *co* (co-polar) is employed; on the other hand, when p and q are opposite polarizations, the term *cross* (cross-polar) is used.
$\Re_{ij}$	Reflection Fresnel coefficient of a signal incident from medium/layer i off the interface with medium/layer j in the MRSR model for dry snow remote sensing.
$\vec{r}$	Spatial vector of the scattering points.
$\vec{r}'$	Spatial vector required for integrating the different points across the reflecting surface.
$s(t)$	Radar baseband signal.
$s_{L1}(t)$	GPS signal at L1 (Blocks IIA and IIR).
$s_{L2}(t)$	GPS signal at L2 (Blocks IIA and IIR).
$S_{C/A}(\kappa) \equiv \chi_{C/A}(0,\kappa)$	Frequency component of $\chi_{C/A}$ for $\tau = 0$.
$S_C(p; p_{ref})$	Cost function that evaluates the overall difference between the lag-hologram resulting from a profile with a perturbation p, compared to a reference density profile with a perturbation p_ref.
t	Time variable.
T	Receiver temperature (antenna + thermal noise).
T_a	Antenna temperature.
T_{LNA}	LNA temperature.
T_c	Equivalent noise temperature of the cable.
T_{eq}	Equivalent noise temperature of the RF front-end.
T_h	Horizontal component of the brightness temperature.
T_v	Vertical component of the brightness temperature.
T_i	Coherent integration time.
$T_M = 70$ seconds	Mean multipath period estimated during Greenland's experimental campaign.
T_{ENU}^{NED}	Transformation matrix from a East-North-Up to a North-East-Down system.

$\mathcal{T}_{ij}$	Transmission Fresnel coefficient where the incident layer/medium is i and the medium into which the signal propagates is j in the MRSR model for dry snow remote sensing.
U_i	Amplitude with which a field that incises into the snow, propagates down to the i-layer, rebounds, and propagates back to the snow-air interface, finally reaches the receiver in the MRSR model for dry snow remote sensing.
V_b	Relative brine volumen (in ‰).
w_d	Complex waveform from direct GPS signals.
w_r	Complex waveform from reflected GPS signals.
$\mathcal{W}(\tau_w, f_I)$	Lag-hologram.
$\overline{\mathcal{W}}(\tau_w, f_I)$	Normalized lag-hologram.
X_ρ^0	1-D array of a-priori snow density profile.
X_ρ	1-D array of snow density profile.
$Y_\mathcal{W}$	1-D array of Lag-Hologram $\mathcal{W}$.
$Y_\mathcal{W}^0$	1-D array of Lag-Hologram obtained by $Y_\mathcal{W}^0 = f_L(X_\rho^0)$.
$Y_\mathcal{W}^{p_{ref}}$	1-D array of modeled Lag-Hologram with a reference perturbation p_ref.
$Y_\mathcal{W}^p$	1-D array of modeled Lag-Hologram with a given perturbation p.
$z(x, y)$	Gaussian height distribution of zero mean ($< z(x, y) >= 0$).
α	Attenuation constant.
α_i	Attenuation constant of the i-layer in the MRSR model for dry snow remote sensing.
β	Azimuth angle, positive clockwise from North ($\beta = 0$).
δ_p	Penetration depth.
Δ_{lag}	Lag-spacing.
Δf_D	Relative Doppler frequency.
ΔH	Residual height.
$\Delta\phi_I$	Residual interferometric phase.
$\Delta\phi_{geo,k}$	Phase increment due to the delay path travelled by the k-reflected signal.
ΔH_{ice}	Height increment due to presence of ice.
ΔH_{tide}	Height variation given by the tide movement.

ΔMSS	Mean square slope increment for MSS-inversion.
$\Delta X_\rho = X_\rho - X_\rho^0$	Residual X_ρ for lag-hologram total inversion.
$\Delta Y_\mathcal{W} = Y_\mathcal{W} - Y_\mathcal{W}^0$	Residual $Y_\mathcal{W}$ for lag-hologram total inversion.
$\epsilon = \epsilon' + i\epsilon''$	Complex relative permittivity.
ϵ'	Dielectric constant.
ϵ''	Dielectric loss factor.
ϵ_{sw}	Relative permittivity of sea water at L-band.
ϵ_{si}	Relative permittivity of sea ice at L-band.
$\epsilon_{ice} = 2.95 + i0.001$	Relative permittivity of pure ice at L-band.
ϵ_{ws}	Relative permittivity of wet snow at L-band.
ϵ_{ds}	Relative permittivity of dry snow at L-band.
ϵ_i	Relative permittivity of dry snow at L-band from i-layer in the MRSR model.
ε	Elevation angle.
θ	Incidence angle.
θ_i	Incidence angle of the i-layer in the MRSR model for dry snow remote sensing.
θ_{BF}	Roll angle.
κ	Doppler frequency.
λ	Wavelength.
$\Lambda_{C/A}(\tau) \equiv \chi_{C/A}(\tau, 0)$	Temporal component of $\chi_{C/A}$ for $\kappa = 0$.
ν	Intrinsic impedance of the medium.
ν_i	Volume fraction of ice in the snow mixture.
ξ_ϕ	Total phase error (non-modeled effects).
ξ_{mod}	Height error coming from the mismodeling of the time-dependent components of $\widehat{\rho_I}$.
ξ_{phase}	Height error coming from the propagation of ξ_ϕ into the linear fitting.
$\xi_{fad/coh}$	Contribution in ξ_ϕ due to impact over the received signal due to fading and coherence loss.
ξ_{mpath}	Contribution in ξ_ϕ due to distortion of the signal due to multipath.
ξ_N	Contribution in ξ_ϕ due to instrumental noise.
ξ_{TZD}	Error in the estimation of D_z (TZD).
$\pi = 3.14159265$	Pi number.
$\rho_{\mathrm{C/A}} \approx 300$ m	Chip-range of the GPS C/A signal.

ρ_{geo}	Geometric range delay.
ρ_s	Snow density.
ρ_{MAX}	Location of the maximum in the waveform.
ρ_{DER}	Location of the maximum in the waveform's first derivative.
$\rho_{scatt} = \rho_{MAX} - \rho_{DER}$	Scatterometric range delay.
ρ_I	Interferometric range delay: difference between the electromagnetic path length of the reflected (R_r) and the direct signal (R_d).
ρ_{curve}	Correction in ρ_I due to the Earth curvature.
ρ_{tropo}	Difference in tropospheric path distance between reflected and direct signals.
ρ^P_{tropo}	Tropospheric delay at a given position P.
ρ_{ant}	Projection of the distance between the antennas along the line of sight.
$\rho_{corr} = \rho_{curve} + \rho_{tropo} + \rho_{ant}$	Correction range delay term.
ρ_M	Range delay between multipath-reflected and direct signals.
ρ_i	Range delay with which a field that incises into the snow, propagates down to the *i*-layer, rebounds, and propagates back to the snow-air interface, finally reaches the receiver in the MRSR model for dry snow remote sensing.
ρ_{int-i}	Range delay-contribution from the internal propagation through the *i*-layer in the MRSR model for dry snow remote sensing.
ρ_{TS}	Range delay from Transmitter to Specular reflection point in the MRSR model for dry snow remote sensing.
ρ_{SR}	Range delay from Specular reflection point to Receiver in the MRSR model for dry snow remote sensing.
ρ_{TR}	Range delay from Transmitter to Receiver (direct radio-link) in the MRSR model for dry snow remote sensing.
$\varrho(x_{corr}, y_{corr})$	Transversal autocorrelation function of height distribution $z(x, y)$.
σ_b	Bistatic radar cross-section (constant).
$\sigma^0_{pq}(\vec{r})$	Bistatic radar cross-section (normalized function) in the pq polarization state.
σ^2_h	Variance of height distribution $z(x, y)$.
$\sigma_{\Delta H}$	Standard deviation of ΔH obtained at the linear fitting (measurement of the formal precision of the estimation).
σ_H	Standard deviation of height estimation.
σ_ρ	Standard deviation of range delay estimation.
τ	Time delay.
τ_0	Duration of a radar's rectangular pulse (pulse-radar).
$\tau_{C/A} = 1/(1.023 \text{ MHz}) \approx 1\mu s$	Chip-duration or chip-width of the GPS C/A signal.

τ_{chip}	Chip-duration.
τ_w	Correlation delay in GOLD-RTR lags (1 lag$\simeq$15 meters).
ϕ_0	Constant phase offset.
ϕ_{L1}	Phase offset from GSP L1 signal.
ϕ_{L2}	Phase offset from GSP L2 signal.
ϕ_I	Complex field's phase.
ϕ_{pq}	Phase of the Fresnel coefficient in the pq polarization state ($\Re_{pq}$).
$\phi_{POPI} \approx \phi_{co} - \phi_{cross}$	RHCP-to-LHCP phase difference of the Fresnel coefficients, or POPI.
ϕ_{pol}	Phase of the polarimetric field C_{pol}.
ϕ_i	Phase of the i-layer contribution with respect to the direct signal in the MRSR model for dry snow remote sensing.
ϕ_d	Phase of the complex waveform from direct GPS signals (w_d).
ϕ_{BF}	Pitch angle.
Φ_M	Multipath phase with respect to the main signal.
$d\Phi_M/dt$	Fading rate provoked by a planar-reflector multipath in the received signal.
$\chi(\tau, \kappa)$	Woodward Ambiguity Function.
ψ_{BF}	Yaw angle.
ω	Angular frequency.
$\widehat{\ }$	Model of a given variable ($\widehat{X}$ would be a model of X).
$\{ENU\}$	Local coordinate reference with the 1-axis pointing towards East, 2-axis pointing towards North and 3-axis pointing upwards.
$\{NED\}$	Local coordinate reference with the 1-axis pointing towards North, 2-axis pointing towards East and 3-axis pointing downwards.
$\{xyz\}$	Aircraft/local body-frame with 1-axis pointing aircraft forward, 3-axis pointing aircraft down and 2-axis forming a direct system.
$\{XYU\}$	Local direct reference frame with the 3-axis pointing upwards and the plane $\{Y, U\}$ contains the transmitter, the receiver and the specular point, with $Y_{transmitter} > 0$.

B

GOLD-RTR MINING: A WEB SERVER OF GNSS-R DATA

GOLD-RTR Mining is a web server for downloading GNSS-R experimental data and related information. In particular, the data collected from 2005 with the GOLD-RTR during the different experimental campaigns carried on by ICE-CSIC/IEEC, including GPS-SIDS at Greenland and Antarctica, whose analysis represents the fundamental core of the present thesis dissertation. Cardellach et al. (2011) provides several examples and tips about the processing possibilities of the whole dataset.

The GOLD-RTR Mining was developed at ICE-CSIC/IEEC as part of this PhD studies with the purpose of sharing the data acquired with the scientific community. The link address of the web server is:

`http://www.ice.csic.es/research/gold_rtr_mining`

A screenshot of the index webpage is shown in Figure 113.

After a free registration process, any identified user can access to the data records. These files are classified into WAV and INT, depending on the type of integration performed upon them. The category WAV refers to waveforms coherently integrated up to 1 msec, thus containing phase information, whereas INT refers to power waveforms incoherently integrated –typically– up to 1 sec. Note that WAV notation is then equivalent to the term RAW introduced in Chapter 3 (INT notation is consistent).

The files contain additional information, such as time-tag, PRN number or antenna's polarization, following the structures described in *Documentation* → *Formats* from the website (although these definitions are given on the files' header also).

Figure 113.: Screenshot of the GOLD-RTR Mining's index webpage.

C

SOFTWARE SYSTEM FOR REMOTE OPERATION OF A GNSS-R SETUP

A software system was developed at ICE-CSIC/IEEC during the preparation of the GPS-SIDS experimental campaigns and as part of this PhD studies, with the purpose of remotely operating the GNSS-R setup described in Chapter 3. Basically, it was required that an operator would be able to download acquired data, upload configuration files to the GOLD-RTR receiver and to monitor the whole system in real time and from a remote location. To do so, it was decided to build an architecture based on Apache Subversion (SVN), a software versioning and revision control system distributed under an open source license (SVN, 2011), with several processes running in parallel in the local terminal unit (TU) and in a remotely located user end (UE) connected trough Internet or a local area network (LAN). The main characteristics achieved under this approach are:

- **Robustness:** Due to SVN transfer election, the system has implicit backups (SVN repositories) and is robust against communication cuts.
- **High data collection performance:** GNSS-R data is collected at TU and then sent to UE to be processed. If a communication cut happens, missing data at UE is again sent once communication is restored.
- **Autonomy:** Given that whole-campaign configurations can be predicted from a single satellites' orbit file, TU has a great autonomy. However, Internet/LAN connection is needed to monitor the data collection and to continuously update the configuration files with more recent orbits.
- **Security:** SVN configuration is password restricted. Direct access to TU via SSH/HTTP connection is password and IP-address restricted.

Figure 114 provides a basic diagram of the software operation setup. Different colors identify those elements belonging to each subsystem, which are described next. The real time monitoring is made by means of a HTTP website located at UE to be accessed anywhere with an Internet connection. A screenshot example is shown in Figure 115.

C.1 CONFIGURATION SUBSYSTEM

Software routine *configure daemon* at UE checks if there is a new igr-file (satellite *rapid* orbits) at IGS FTP server (IGS, 2013). In that case, it makes an estimation of the configuration files and updates the SVN inputs repository for the next 7 days. In addition, whole experiment configurations are monthly done using the latest satellite positions, enabling

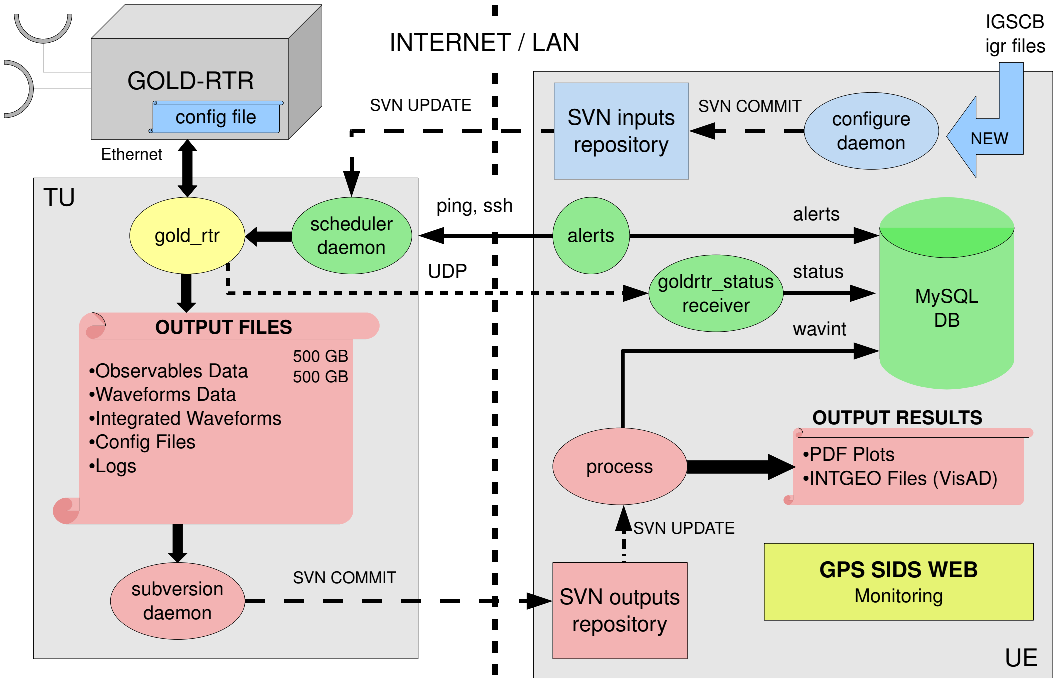

Figure 114.: System's Architecture for remote operation of a GNSS-R setup. Different colors identify those elements belonging to each subsystem: [blue]-Configuration, [green]-Control&Communications and [red]-Processing.

then a long configuration autonomy in case of connection loss between UE and TU. User configuration (non-automatic) is also permitted by updating the SVN inputs repository. SVN offers a control of changes into the configuration files, allowing their tracking in an easy way.

C.2 CONTROL&COMMUNICATIONS SUBSYSTEM

The basic control of the collected data is done by means of the configuration files, which are automatically generated. The process *scheduler daemon* at TU continuously updates an inputs-workspace, and make calls to *gold_rtr* process depending on the different configuration files. For each call, process *gold_rtr* charges a new configuration in the GOLD-RTR, and a new experiment begins. Given that this process should be working all the time, a *crontab* is scheduled to periodically awake it. In addition, real time status flags are sent by *gold_rtr* process every second with an UDP message to UE.

A SVN server at UE controls data storage and timing. An *alerts* process checks Internet/LAN connection, data availability, etc., generating alert records and storing them in the MySQL database (DB). Similarly, process *goldrtr_status* checks the status flags sent by *gold_rtr* and stores them also in the MySQL DB. In case of some incidence, the operator at UE can then access to the remote TU via SSH and reactivate the system (if there is Internet/LAN connection). It is also possible to do a remote hardware reset of GOLD-RTR and TU via a web-based power supply. The router at TU is programmed to keep security by cutting intrusive SSH/HTTP connections.

C.3 PROCESSING SUBSYSTEM

At TU, *gold_rtr* gets the data from the GOLD-RTR via an Ethernet connection. For each experiment, RAW data, INT data, log and configuration files are saved in a given folder structure called outputs, which is a work-copy of the SVN repository. Process *subversion daemon* continuously checks if output files are finished. Then, it compresses INT files (*bzip2*) and commits the changes to the outputs SVN repository. RAW data is not transmitted due to a data transfer rate limitation (40 GB/month).

At UE, *process daemon* checks the changes into the outputs SVN repository, processing the new files when they are received. Firstly, it checks if output files are coherent with the corresponding configuration (storing this information into the MySQL DB); secondly, it makes plots (in PDF) of the collected waveforms for monitoring purposes; and finally, it generates INT files with positioning information when the corresponding satellite orbits are available (typically after 2 days).

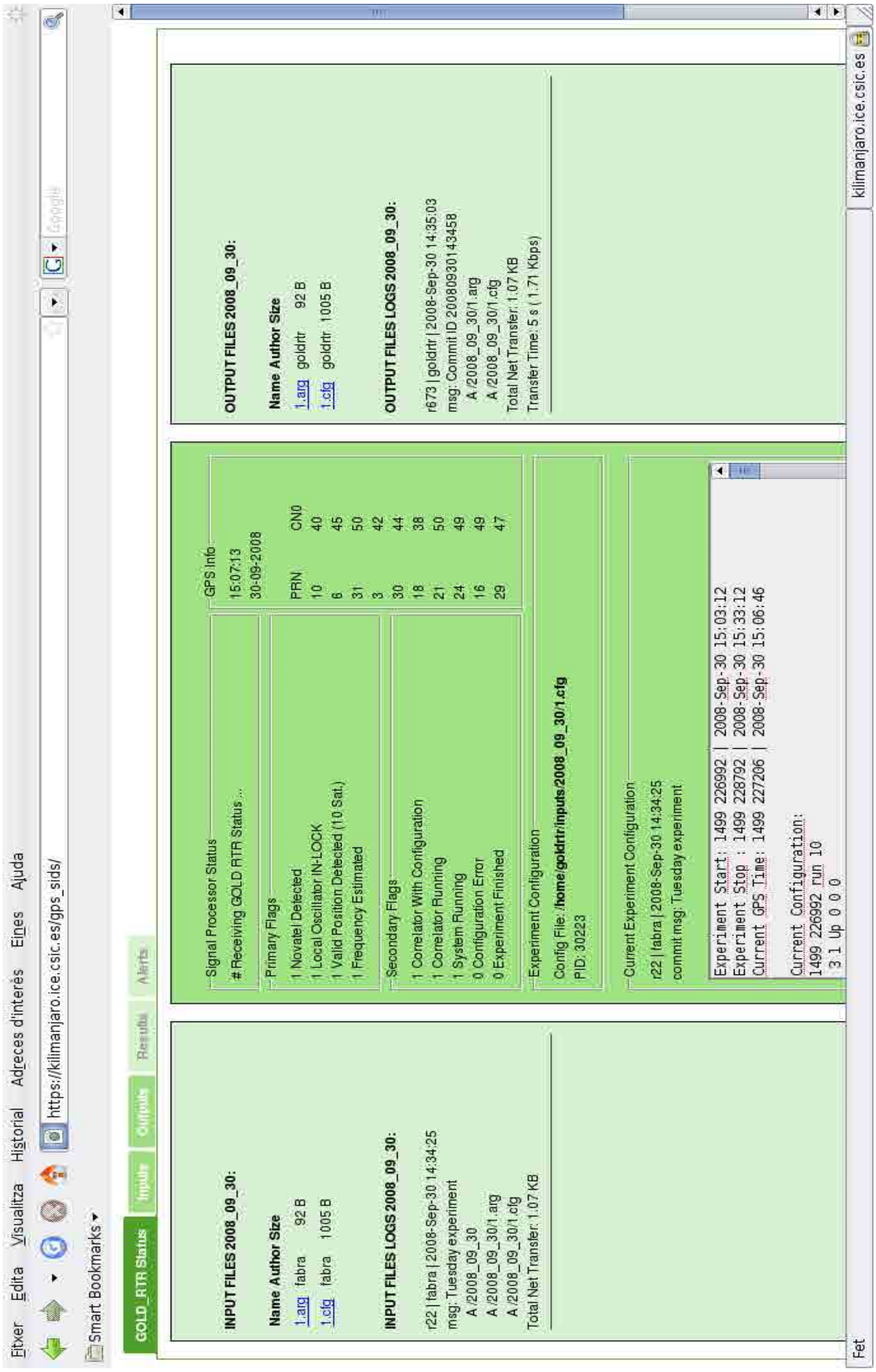

Figure 115.: Screenshot of the Web-based monitoring system for GPS-SIDS.

D

ANCILLARY DATA FROM GREENLAND'S CAMPAIGN

D.1 METEOROLOGICAL OBSERVATIONS FROM ARCTIC WEATHER STATION

During the experimental campaign, meteorological records measured from a nearby ground Arctic Weather Station (53.516°W, 69.253°N) were provided by DMI. The location of this weather station is displayed in Figure 24. Time series of the observed pressure, temperature, relative humidity and precipitations are displayed in Figure 116. In addition, a more relevant parameter for this study such as sea ice concentration was also provided. It was obtained by means of visual inspection and its evolution is shown in Figure 117.

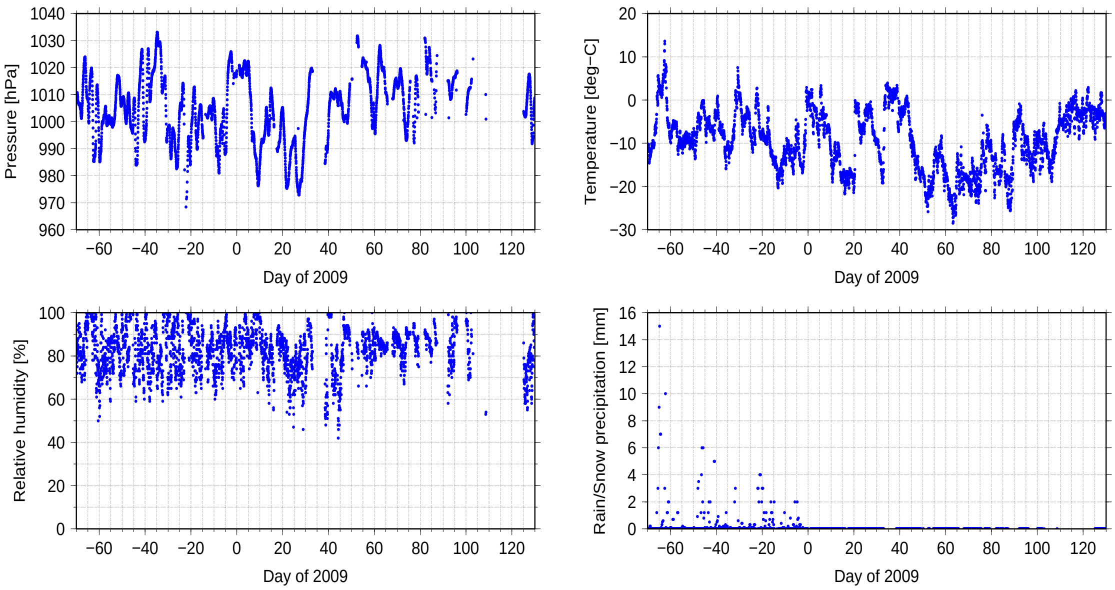

Figure 116.: Time series of the atmospheric pressure (top-left), temperature (top-right), relative humidity (bottom-left) and rain/snow precipitation (bottom-right) measured at the Arctic Weather Station.

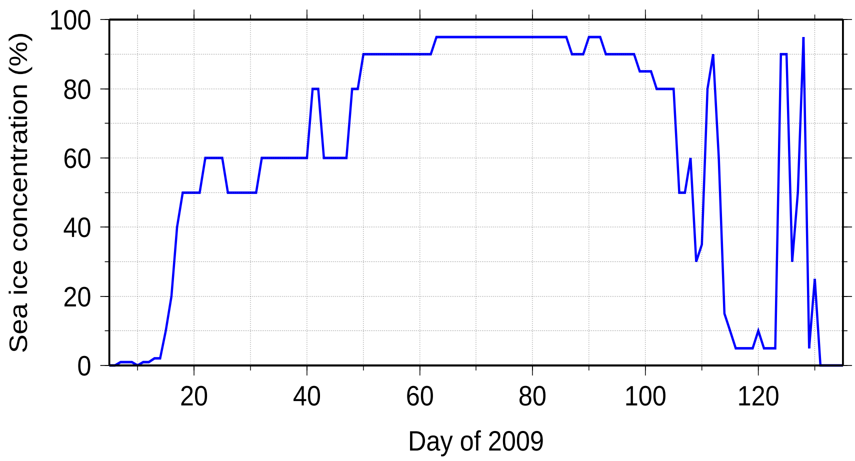

Figure 117.: Sea ice concentration as visually estimated from Arctic Weather Station.

D.2 TOTAL ZENITH DELAY

The microwave signals on the two carriers L1 and L2 in the GHz band broadcasted by the GPS satellites are delayed by the ionosphere and the neutral atmosphere on their way to the ground receiver. The ionospheric refraction is dispersive and is usually corrected using both frequencies to obtain the **ionosphere-free linear combination**, which is a standard observable for geodetic applications. Moreover, it affects almost identically both direct and reflected radio-links, thus canceling when subtracting both signals. The refraction in the neutral atmosphere is not dispersive and its value cannot be taken directly from dual-frequency measurements. It can only be derived by estimation techniques along with other parameters. The **neutral** refraction is mainly induced by dry air, water vapor, clouds and rain, and is proportional to the masses of the specific components along the ray path. The delay is smallest in the direction of the zenith and increases approximately with the reciprocal of sine of the elevation angle ε. The elevation dependence is described by a mapping function. The total atmospheric delay ρ_{tropo}^{Rx} contained in a GPS observation at the receiver's (Rx) position can be partitioned into two parts (Niell, 1996):

$$\rho_{tropo}^{Rx} = m_{hz}(\varepsilon) \cdot D_{hz}^{Rx} + m_{wz}(\varepsilon) \cdot D_{wz}^{Rx} \tag{116}$$

where D_{hz} is the zenith hydrostatic delay, D_{wz} the zenith wet delay, m_{hz} the hydrostatic mapping function and m_{wz} the wet mapping function. The total zenith delay (D_z) is the sum of D_{hz} and D_{wz}. The delay in the dry air (the hydrostatic component) is proportional to the air masses and amounts to $\sim$2.5 m for measurements in the zenith. The delay from the water vapor has a much higher variability and it ranges from a few mm in arid regions to 400 mm in humid regions. The refractivity caused by water vapor's permanent dipole is per mole about 17 times that of dry air. Typically, the influence of clouds and rain are marginal, and cannot be computed from the GPS measurements. For extreme weather conditions their influence may reach 10% in D_{wz}, normally it is smaller than 5% (Solheim et al., 1999).

The total zenith delays observed during the campaign were successfully processed by GFZ using the data acquired by the geodetic receiver. They are displayed in Figure 118, along with the zenith delays corresponding to the atmosphere modeled by the ECMWF numerical weather model (NWPM), showing its good agreement. The wet component is detailed in Figure 119.

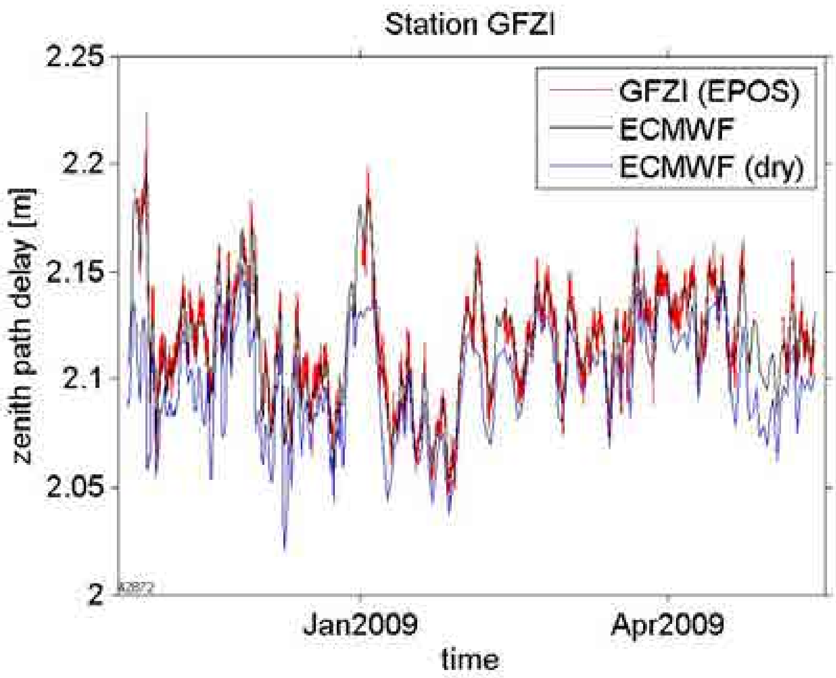

Figure 118.: Total Zenith Delay observed by GFZ's geodetic receiver, together with the NWPM values (ECMWF model). Plot provided by GFZ.

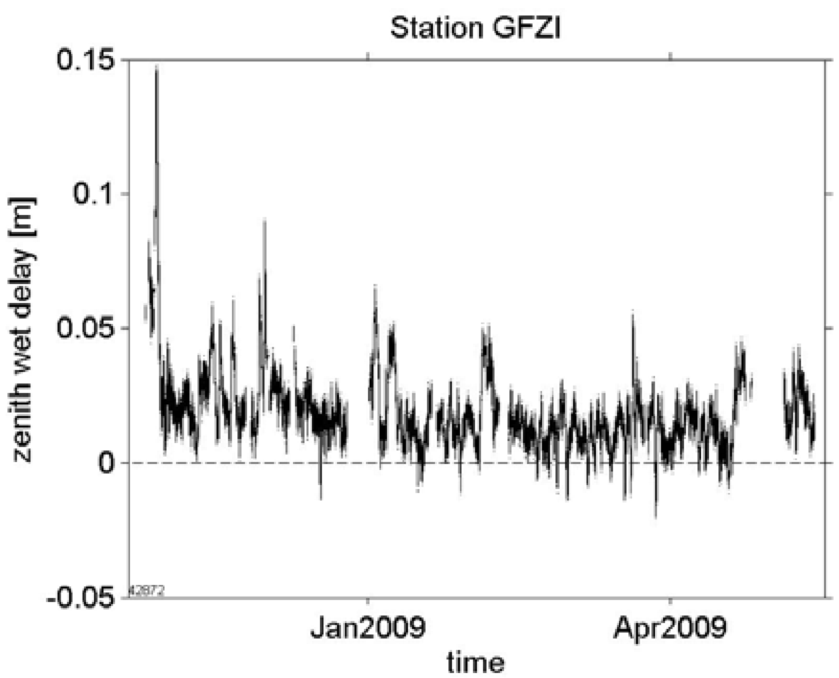

Figure 119.: Wet component of the zenith atmospheric delay, observed by GFZ's geodetic receiver. Plot provided by GFZ.

D.3 POLAR ICE CHARTS

The Centre for Ocean and Ice at DMI regularly produces ice charts covering the Greenland Waters by combining in-situ with remote sensing measurements (PV-DMI, 2013). The ice charts are produced mainly to support navigation around Greenland, so their resolution is lower than the desired for the experimental site. Despite of that, all the available ice charts during the campaign were collected for the data analysis. An example is shown in Figure 120. The *egg-code* of the different areas provides information on three concepts: concentration, development stage (related to thickness), and form (floe size). The concentration is given in percentage, while the phase and form respond to a numeric code, detailed in Table 24.

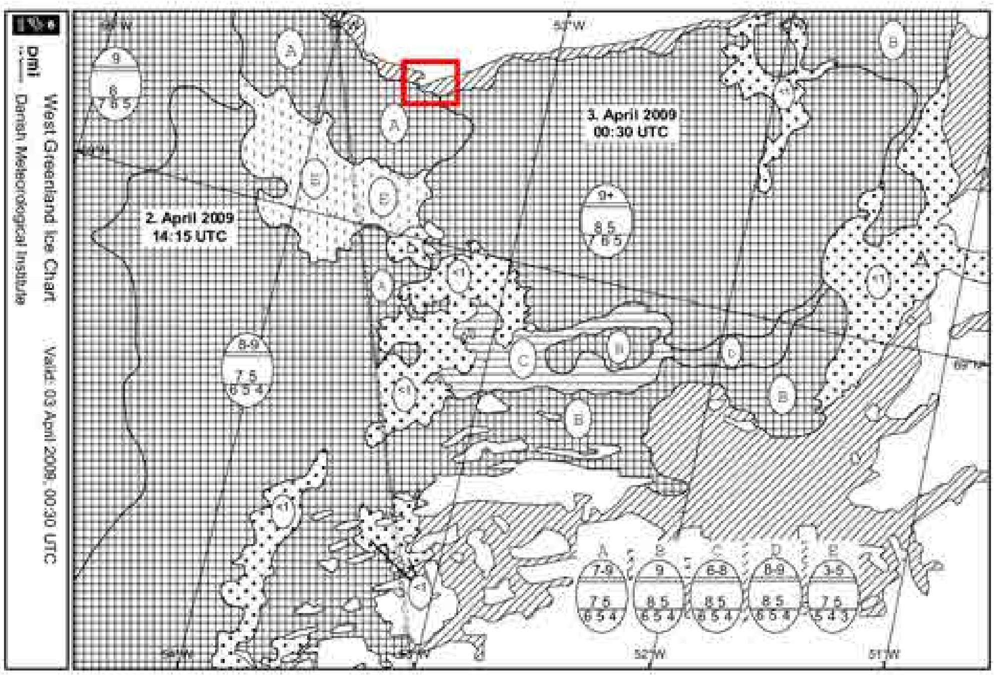

Figure 120.: An example of ice chart provided by DMI from April 3rd, 2009. The approximated monitorization area of the GNSS-R experiment is marked with a red square.

The egg-code may give more than one numerical value per each concept. The black and white ice charts were rotated -14.9° to bring the meridians parallel to the Y-axis, and cropped between longitude 54°W and 53°W, latitude 69°N and the crossing between meridian 53°W and the coast line. Around the experimental site, egg-code information was converted into hexadecimal notation of a given color code by reducing each of the concepts (concentration, stage, and form) to two values, and inserting these two values in the first and second (concentration), third and fourth (stage), and fifth and sixth (form) digits of the hexadecimal code. When more than two values were given for a particular concept, the extremal ones were selected (Figure 121). An example of edited (rotated, cropped, colored) chart is displayed in Figure 122.

CODE	STAGE thickness	FORM floe size
0	ice free	pancake ice
1	new ice	small growlers
2	thin ice (<10 cm)	growlers (<20 m)
3	young ice (10-30 cm)	small floe (20-100 m)
4	10-15 cm	medium floe (100-500 m)
5	15-30 cm	big floe (500-2000 m)
6	winter ice (30-200 cm)	vast floe (2-10 km)
7	30-70 cm	giant floe (>10 km)
8	30-50 cm	fast ice
9	50-70 cm	icebergs

Table 24.: Sea ice egg-codes for development stage and form used in the DMI ice-charts that might appear in the region of the experiment.

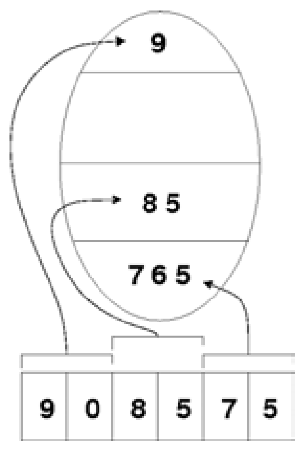

Figure 121.: An example of sea-ice egg-chart transformed into a hexadecimal color code. From up to bottom, code numbers (listed in Table 24) for different characteristics of sea ice: concentration (in %/10 scale), development stage, and form.

Figure 122.: Edited egg-chart: rotated to align parallels with X-axis; cropped into a fixed ares (the same for every plot); egg-chart information around the experiment site transformed into hexadecimal color (example from March 27 2009).

The ground tracks of the GNSS-R observations were then interpolated into the edited colored maps to extract the three concept values at each area of the track. For each PRN, it was then possible to generate three global campaign plots (one for each sea ice characteristic) to be then compared to other GNSS-R derived parameters. An example of global campaign plot is shown in Figure 123 (the way of how is made this type of representation is illustrated in Figure 67). The available ice-charts covered most of the campaign (after ice formation), with typical gaps of 3 days. The values of one day were extrapolated up to three days forward, leaving blank the gap length beyond the third day.

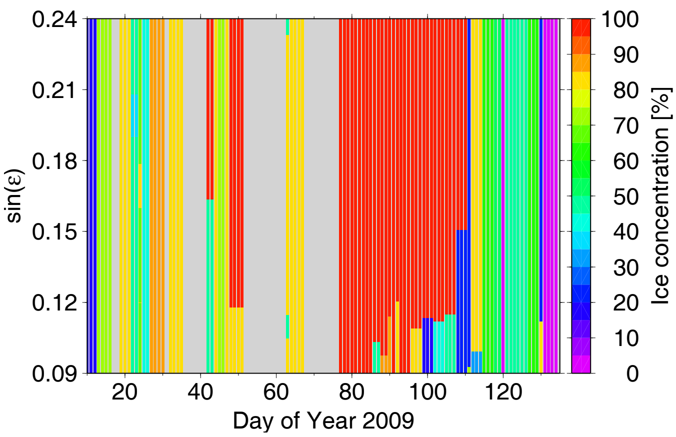

Figure 123.: Example of global campaign plot derived from a DMI's ice chart: sea ice concentration interpolated to PRN02 ground-tracks.

A particular case for this study is given when the egg-code indicates *fast ice* in the ice charts. Fast ice is defined as sea ice that has frozen along coasts (fastened to them) along the shoals, or to the sea floor over shallow parts of the continental shelf, that extends out from land into sea. Unlike drift ice, it does not move with currents and wind. However it still moves with the tides, contributing then to the development of cracks and fissures in the ice cover and therefore, increasing the surface's roughness, which is a key parameter for sea ice classification with GNSS-R employed in Belmonte et al. (2009).

D.4 ICE SURFACE TEMPERATURE FROM MODIS

The ice surface temperature controls the rate of sea ice growth by means of the heat transfer at the ice-water interface (Tucker et al., 1992). This parameter is measured by the Moderate-Resolution Imaging Spectroradiometer (MODIS) (Hall et al., 2009) and can be obtained from NASA WIST server (now *Reverb* (NASA, 2013)). The accuracy of these measurements is 3.0 K with 4 km resolution (Hall et al., 2004).

A set of samples were available at the experimental site during the campaign. The pixel's location is shown at the top panel in Figure 124, whereas the time evolution of their average value is given on the bottom panel.

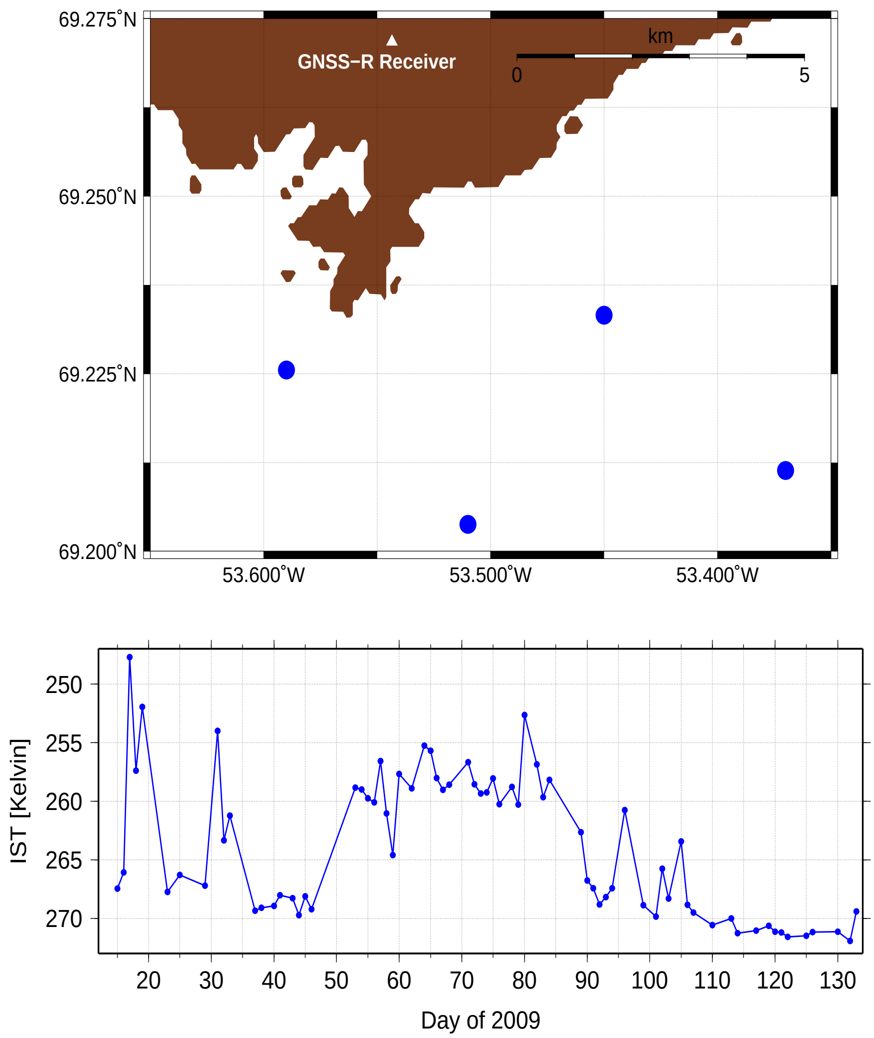

Figure 124.: [Top] Position of MODIS' data samples at the experimental site. [Bottom] Time series of ice surface temperature from MODIS after averaging the available pixel values.

D.5 ALTIMETRIC RETRIEVALS FROM GLAS

As explained in Chapter 2, accurate altimetry over Polar ocean scenarios may help to determine the free-board level of the ice sheets, which in turn is related to their thickness, a key parameter for sea ice characterization. A ground track from the Geoscience Laser Altimeter System (GLAS) from ICESat passes through the experimental area (top panel in Figure 125). Unfortunately, only one coincidence in time for the whole campaigns' period was available (96th day of year 2009), disabling the possibility of a proper statistical analysis. The time search was extended to 2005 in order to increase the historic record and have a better idea about the range of altimetric measurements expected in the area.

The bottom panel in Figure 125 shows the results of the different GLA13 (Zwally et al., 2009) products found plotted with respect to latitude. These height measurements include tidal and atmospheric corrections and an additional software tool has been used for converting the reference ellipsoid from TOPEX/Poseidon to WGS84. Their single-shot error budget has a RSS (residual sum of squares) of 13.8 cm (Zwally et al., 2002). The data-sets and the software tools to work with them were obtained from NASA WIST server (now *Reverb* (NASA, 2013)).

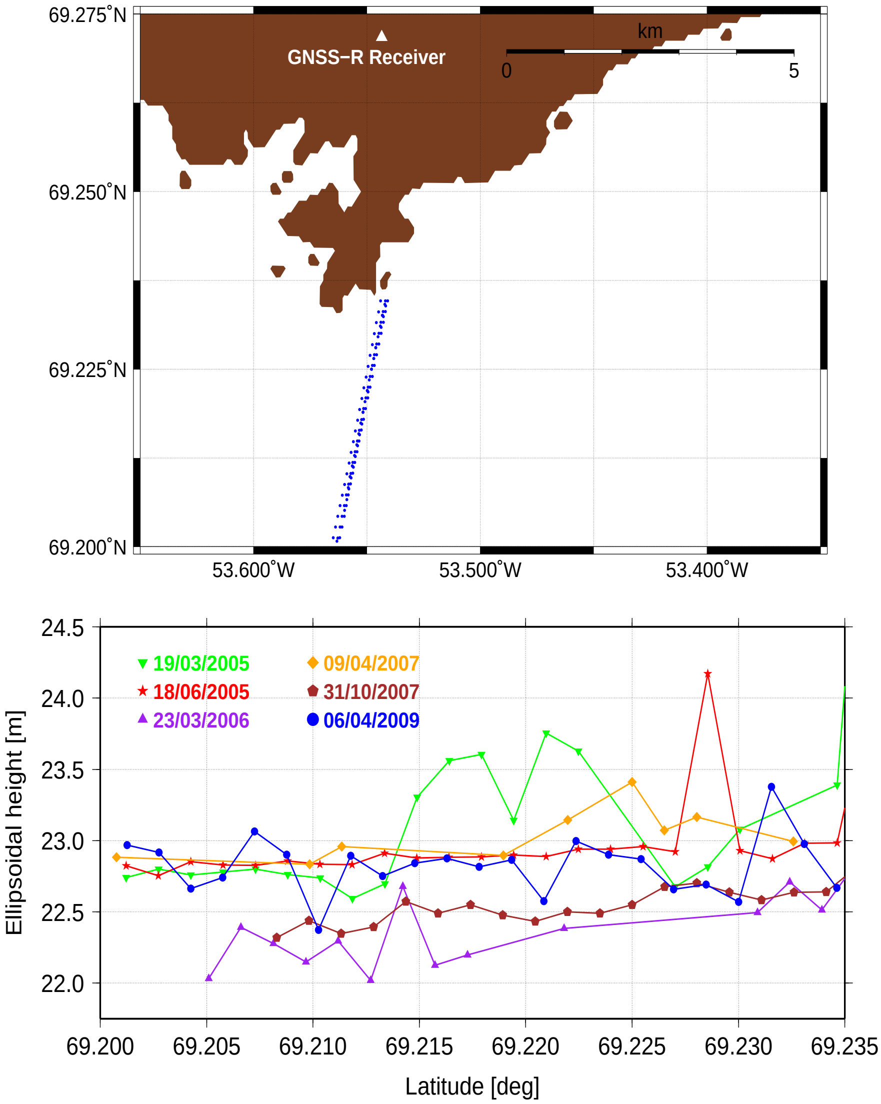

Figure 125.: [Top] Position of GLAS' ground tracks at the experimental site. [Bottom] Height retrievals from ICESat GLAS at the campaign's location for several days. The reference ellipsoid is WGS84 in all cases. Tides effects are corrected. Note that only one track was time-collocated with the GNSS-R experiment.

D.6 ARCTIC TIDE MODEL

In order to retrieve information from the evolution of the sea ice cover from altimetric measurements, the variations of the surface level given by the ocean tide have to be corrected. In absence of in-situ tide gauges, the best option is to use a proper model. For this study, AOTIM-5 (Padman and Erofeeva, 2004) has been employed, a 5-km regular grid regional assimilation tide model of the entire Arctic Ocean. Figure 126 shows the estimation made by the model during several days of the campaign at the experimental site. Notice that the variation with respect to the mean sea level is quite significant in this area, with daily differences up to 2 meters.

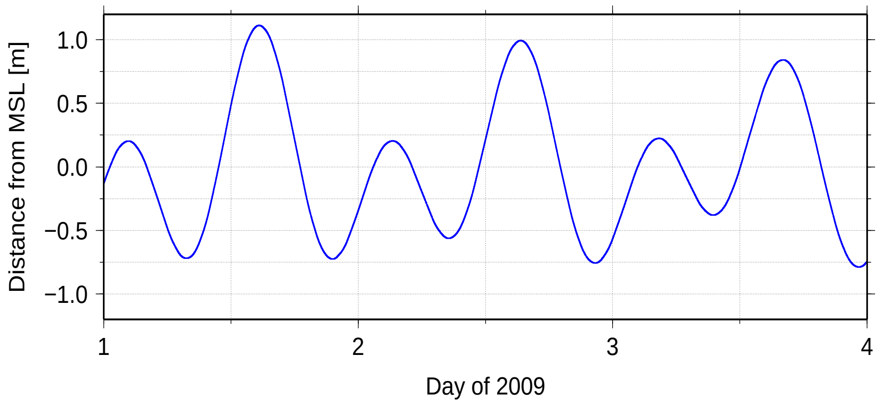

Figure 126.: 3-day example of time evolution of the sea surface level estimated by AOTIM-5 model at the experimental site.

D.7 WIND MEASUREMENTS FROM QUIKSCAT

The wind has an important impact on the roughness of the ocean surface, and therefore, on the shape of the waveforms from reflected electromagnetic signals with a wavelength number comparable to the scale of this roughness, as in the case of L-band ($\sim$20 cm). Wind speed retrievals were provided from the Quick Scatterometer (QuikSCAT) (Dunbar et al., 2006). The land mask applied, which enters 50 Km into the sea, obliges to take measurements away from the experimental area, as it can be seen on the top panel in Figure 127. In addition, these wind retrievals are only available in absence of sea ice. Despite of that, this data-sets can be used to test the roughness' analysis procedures when using GPS reflections taken at open waters. The time evolution of QuikSCAT's wind speed product is shown on the bottom panel in Figure 127.

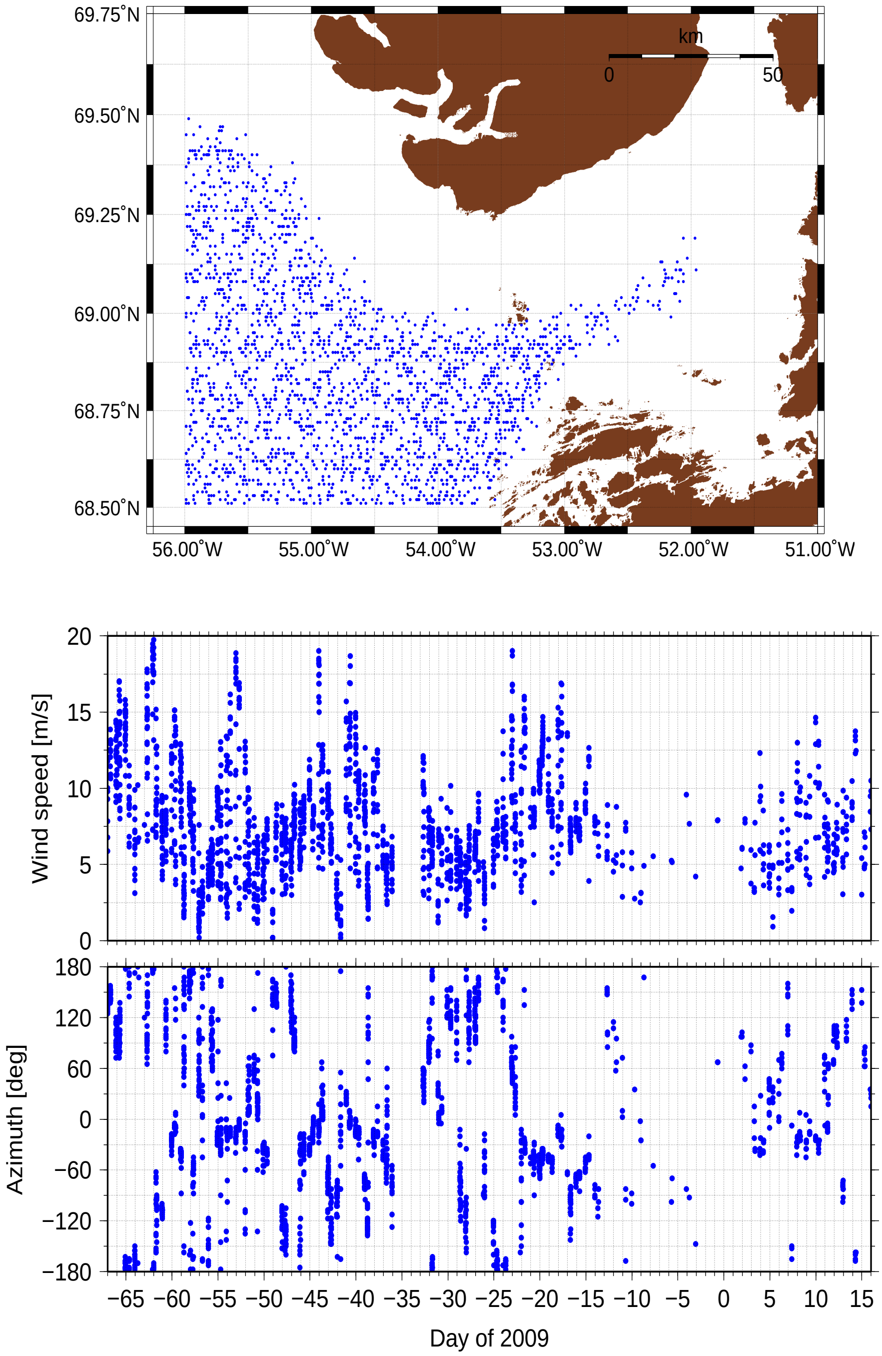

Figure 127.: [Top] Position of QuikSCAT's data samples closest to the experimental site. A land mask of 50 Km is applied. Time series of wind speed [center] and wind direction [bottom] measurements from QuikSCAT.

D.8 PALSAR IMAGERY

High resolution Radar imagery from satellite is especially useful for characterizing sea ice extensions. A few images from the Phased Array type L-band Synthetic Aperture Radar (PALSAR) onboard ALOS were provided by ESA (Rosenqvist et al., 2007). Figure 128 shows the product with highest contrast, HH-pol backscattering coefficient (Horizontal polarization transmitted and received), for all the available days. The presence of thin sea ice is related to the lowest values of this coefficient (Wakabayashi and Sakai, 2011). Like in the case of GLAS, to have obtained more PALSAR images would have been an excellent opportunity for improving the analysis of our data-set, since this instrument works in the same frequency band than GPS and has a decent resolution for our experimental area (<100 meters). At least, these pictures give a proof of the spatial variability of the sea ice cover, showing that ice-water transitions might be expected along a 5 Km ground track.

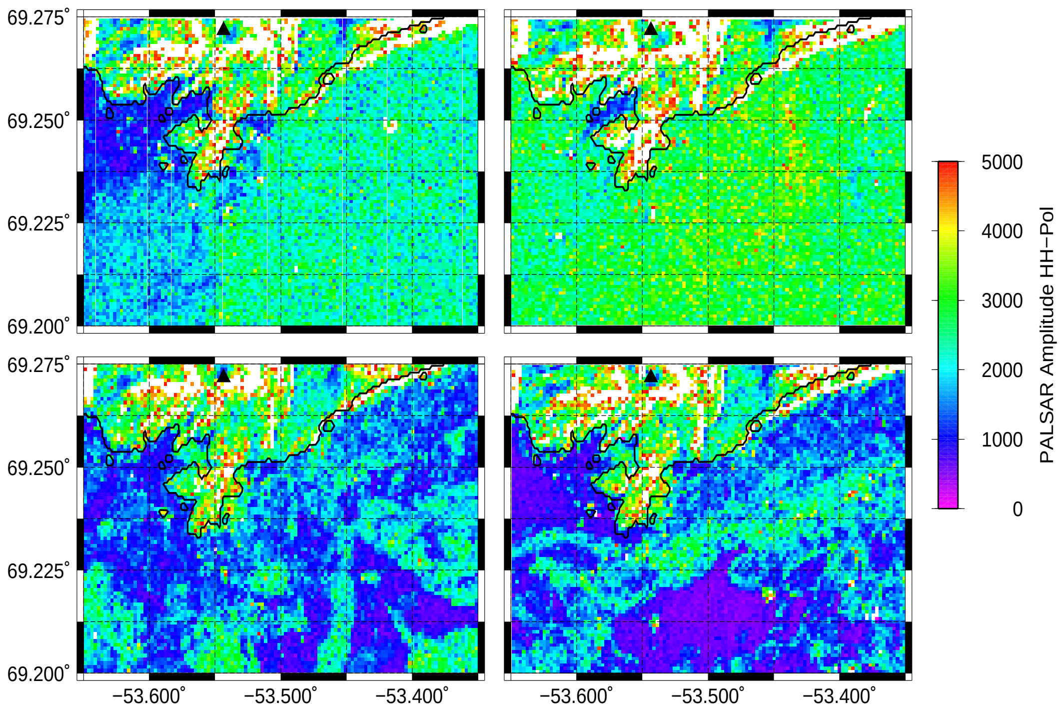

Figure 128.: Polarimetric images from ALOS' PALSAR taken at Disko Bay for different days of the campaign: [Up-Left] December 14th, 2008; [Up-Right] December 19th, 2008; [Down-Left] January 19th, 2009; [Down-Right] January 24th, 2009. The product shown is the HH-pol backscattering coefficient, which provides the highest contrast. The presence of thin sea ice is related to the lowest values of this coefficient (Wakabayashi and Sakai, 2011).

E

ANCILLARY DATA FROM ANTARCTICA'S CAMPAIGN

E.1 ATMOSPHERIC DATA

Atmospheric measurements were obtained from the official AWS (Automatic Weather Station) installed on Concordia base (PNRA, 2013). Air Temperature is represented in Figure 129. The situation is typical of the peak Austral summer, when the average air temperature value lies around -32°C, showing a daily fluctuation of around 12°C with a minimum and a maximum of the period of -43°C and -23°C respectively.

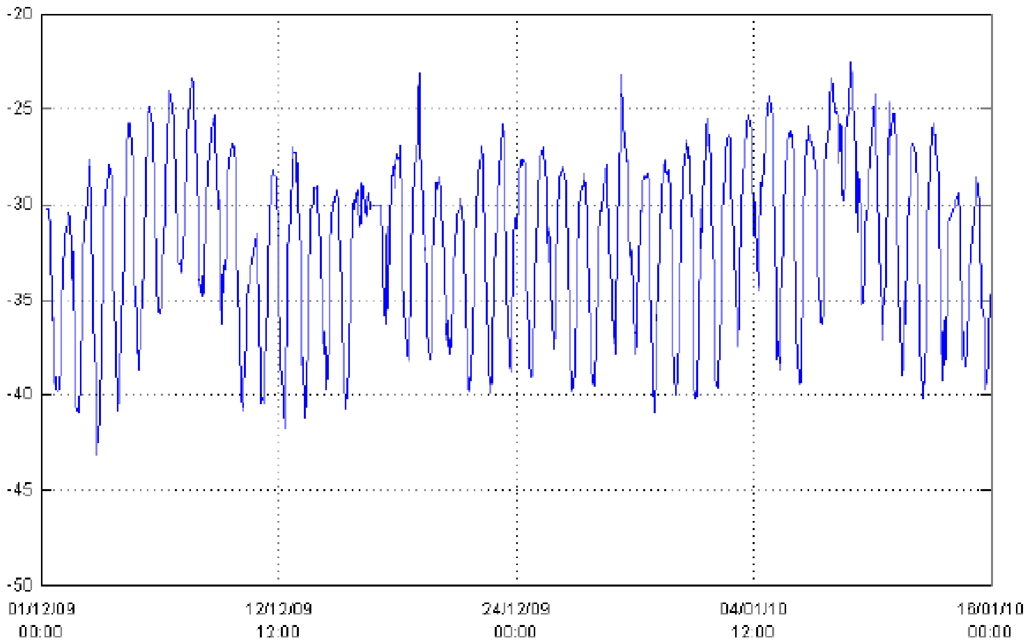

Figure 129.: Air Temperature (°C) measured by the AWS at Concordia Station from 1/12/2009 to 15/01/2010. Plot provided by IFAC.

Wind speed and wind direction are represented in Figure 130. We can observe that wind speed was in general very low and showed a typical value below 10 kts, with some exceptional peaks (e.g. 6-7/12 and 5-8/01) where wind speed reached values higher than 30 kts. Wind direction ranged from North-West to East.

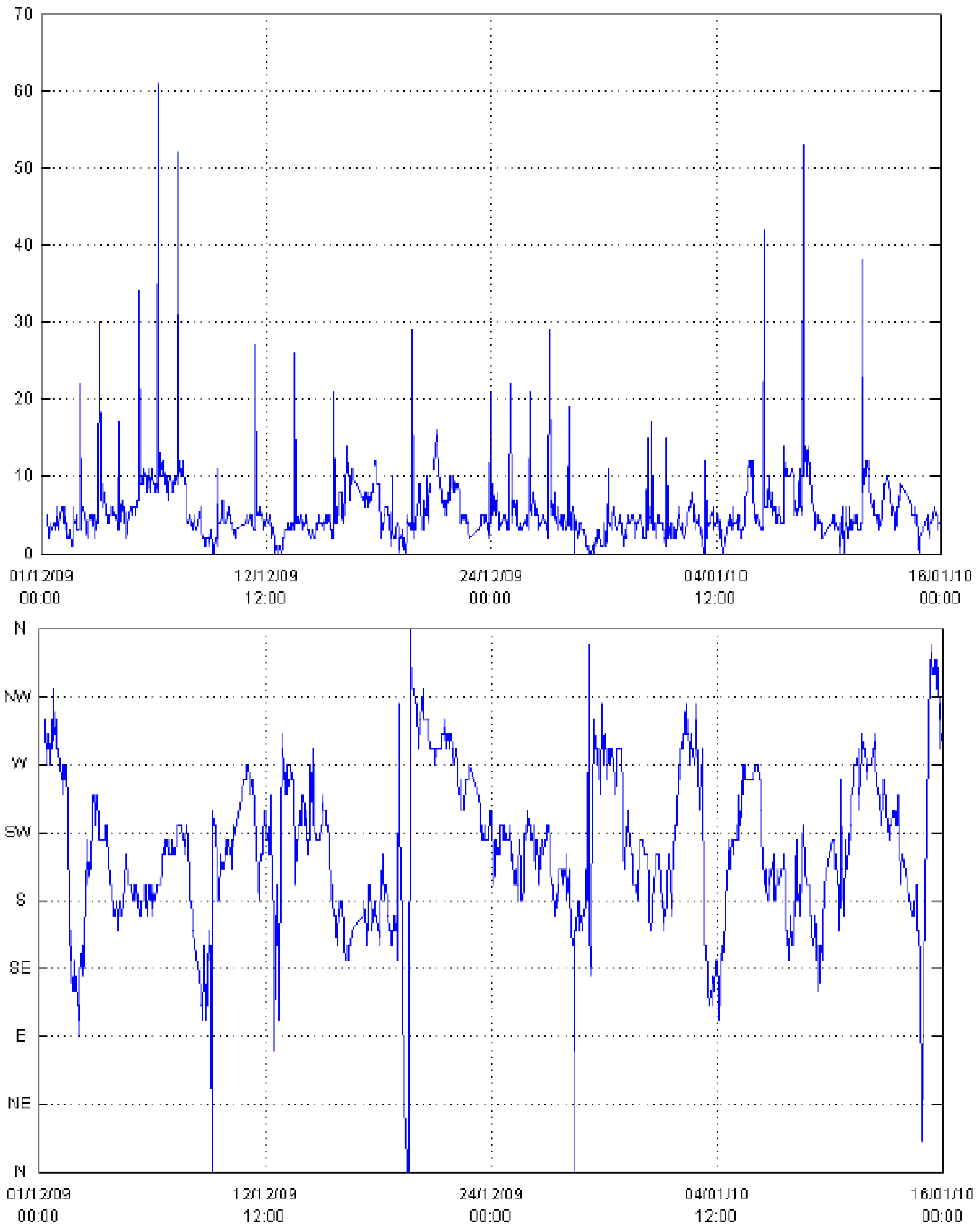

Figure 130.: [Top] Wind speed (kt) and wind direction [bottom] measured by the AWS at Concordia Station from 1/12/2009 to 15/01/2010. Plots provided by IFAC.

E.2 SNOW TEMPERATURE

These measurements started during DOMEX-1 experiment in 2005 and data were continuously acquired until end of 2009. Due to the installation of a series of new nearby shelters during summer 2009, the probes that measure snow temperature in the first 10 meters were removed. For technical and scientific reasons, the shelter called **Helene** near to the American tower was selected as new site (see location in Figure 27). The probes were then removed from their original location and a new 10 m hole was drilled (IFAC in cooperation with LGGE), causing a lack of data from December 2009 to mid of January 2010.

The final setup consists of 10 thermistors embedded in the snow at different depths down to 10 m. The first 4 probes were installed in a 1-meter pit at 5, 10, 50 and 100 cm deep. They are annually controlled and, due to the annual snow accumulation, repositioned to the original depth. The other probes, with a depth interval between 200 and 1000 cm, were installed in a hole closed by a plastic cover. At the beginning of the experiment, the cover was placed 1 m deep. The snow accumulation is measured each year (i.e. the distance from snow surface to the cover) and the depth of the probes is then derived.

Data acquired from 1/01/2010 to 30/01/2010 are represented in Figure 131. Snow temperature oscillated in the first 25 cm due to the forcing of daily air temperature variation and become stable at around 1 meter deep. The temperature profile was typical of the summer season showing maximum values near to the surface and decreasing with depth up to around 5 meters where reached the mean annual value of -55°C. Similar values are expected for the days of the GNSS-R experiment.

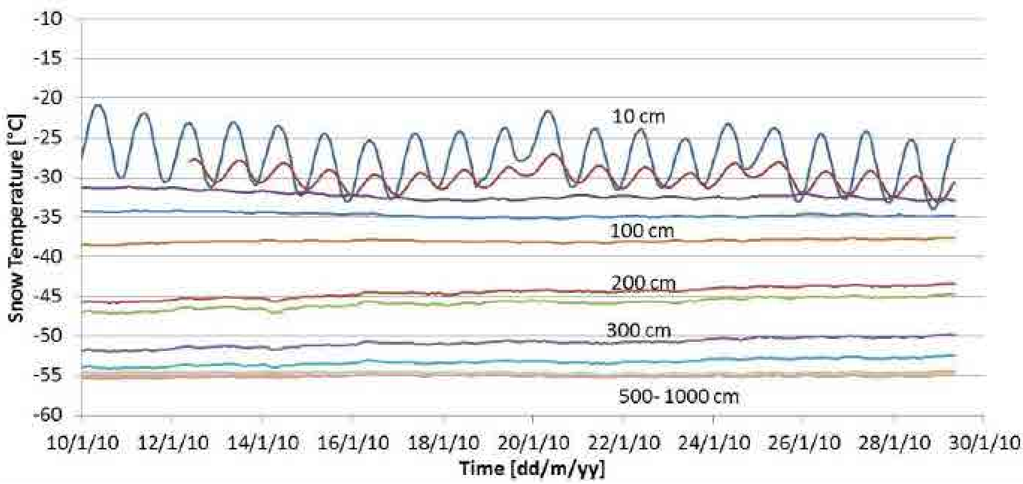

Figure 131.: Snow Temperatures measured at different depths at Concordia Station from 10/01/2010 to 30/01/2010. Note that it was after the GNSS-R campaign completed. Plot provided by IFAC.

E.3 SNOW DENSITY

Contemporaneously to the tower observation experiment, other field activities were performed in order to characterize the ice-sheet properties in the first meters below the surface. This activity was conducted by IFAC in cooperation with scientists from LGGE, which have performed similar and complementary measurements in the snow pits. Up to 14 sites were analyzed and 25 snow pits digged from nearby locations: 20 down to 1 m deep, 4 down to 2 m deep, and 1 at 5 m deep. In particular, a main 5 m pit was dug near the observation tower and stratigraphy of the snowpack was analyzed. In order to characterize the spatial variability of the ice-sheet structure, other snow pits (of around 1 m depth) were digged in the direction NW-SE at 12 Km and 25 Km far from the base. The following parameters have been considered for each snow layer: shape and size of grains (Colbeck et al., 1990), temperature, hardness and density. Dielectric constant of snow was also measured each 10 cm using an electromagnetic probe called Snow Fork (Sihvola and Tiuri, 1986).

The snow analysis included the identification of different snow layers, grain type (shape, size), density of different snow layers. Figure 132 presents an overview of the measured snow density at four different depths and different areas located around the Concordia station. As it can be seen, the higher percentage of measurement lie within the first meter, while few data were collected in the second meter or more.

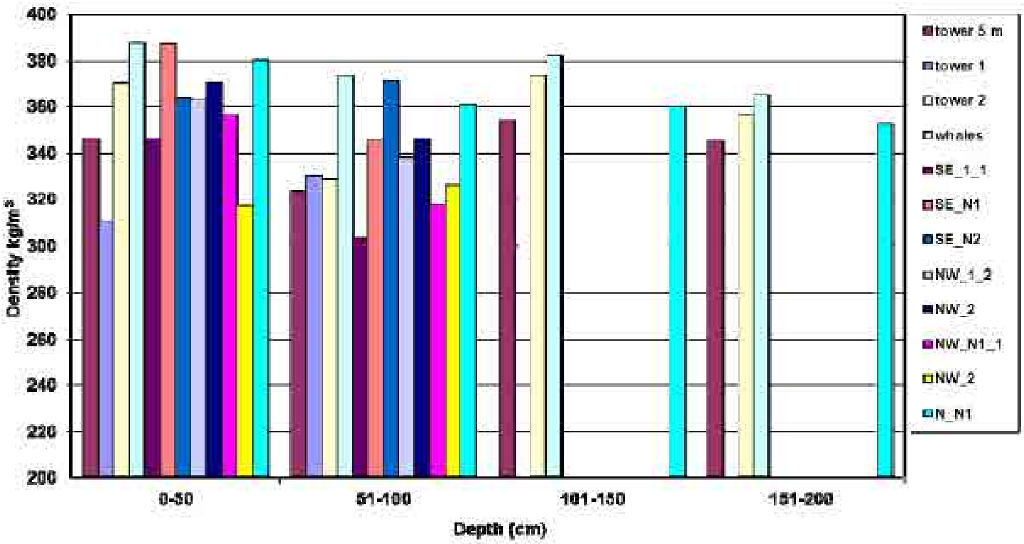

Figure 132.: Density of different snow pits executed in different areas around the Concordia base. Plot provided by IFAC.

The deeper snow pit (5.3 meters) was executed near the American tower, and a synthesis is presented in Figure 133. The top panel shows the trend of the snow density every 50 cm. As it can be seen, some different densities can be observed in the first meters, while the density gradient is homogeneous at deeper layers. The bottom panel shows the comparison of snow density every 10 cm in two different times: 2004 and 2009. Again, different layer densities can be observed in the first meters, while the profiles tend to be similar as the depth increases.

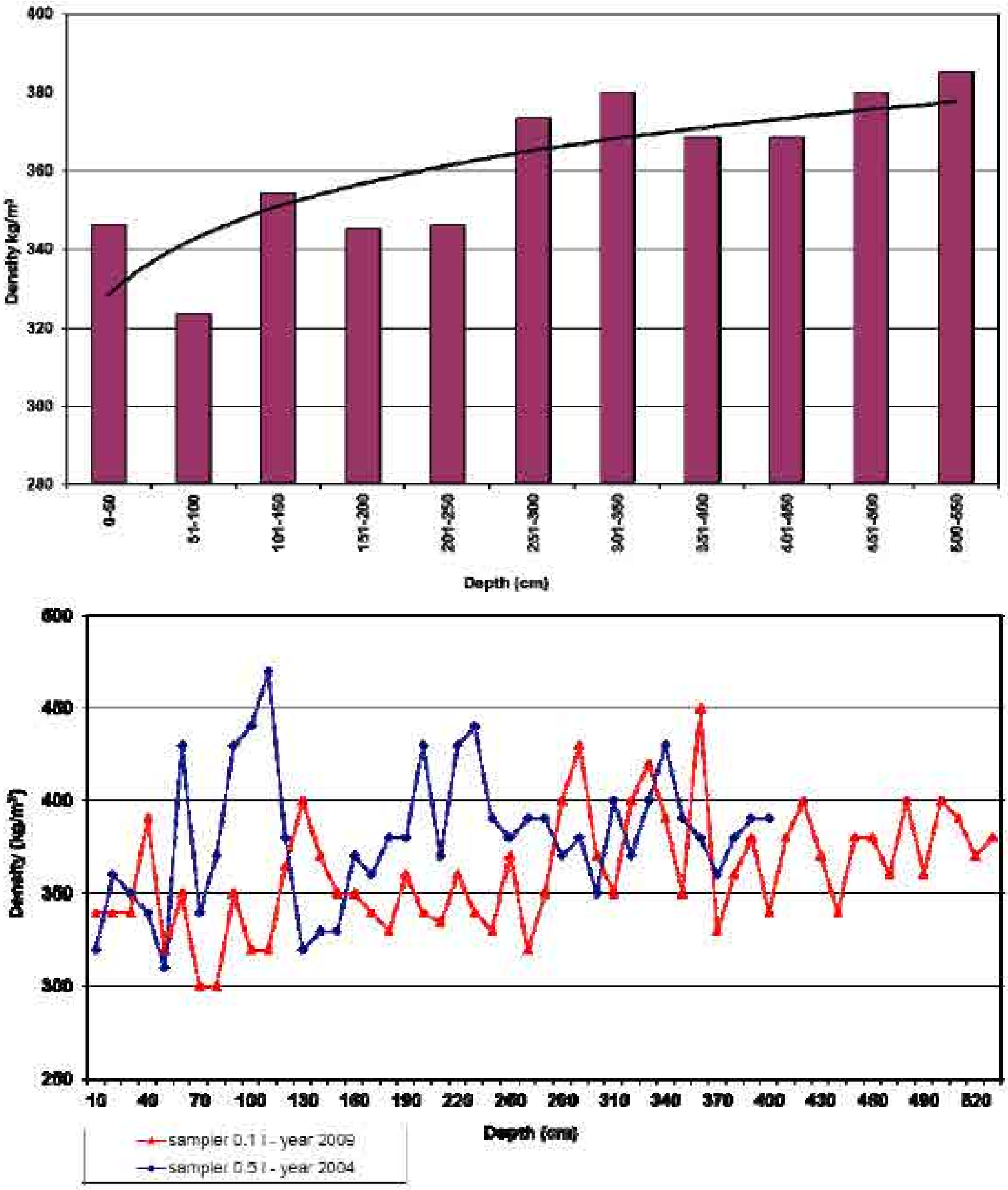

Figure 133.: Mean snow density retrieved every 50 cm [top] and comparison with the results obtained in 2004 campaign [bottom]. Plots provided by IFAC.

In order to get a deeper profile of snow layers, these snow pit measurements were combined with data derived from ice cores (EPICA, 2004), arriving down to 700 meters in the **heart** of Antarctica from Dome-C. The whole snow density profile is shown in Figure 134. Overall, we can see that densities are very low at the surface layer, of the order of ∼0.3 gr/cm^3, presenting several sharp transitions of ±0.2 gr/cm^3 during the first 10 meters depth, to gradually increase up to a saturation value of 0.92 gr/cm^3 starting at ∼250 m depth.

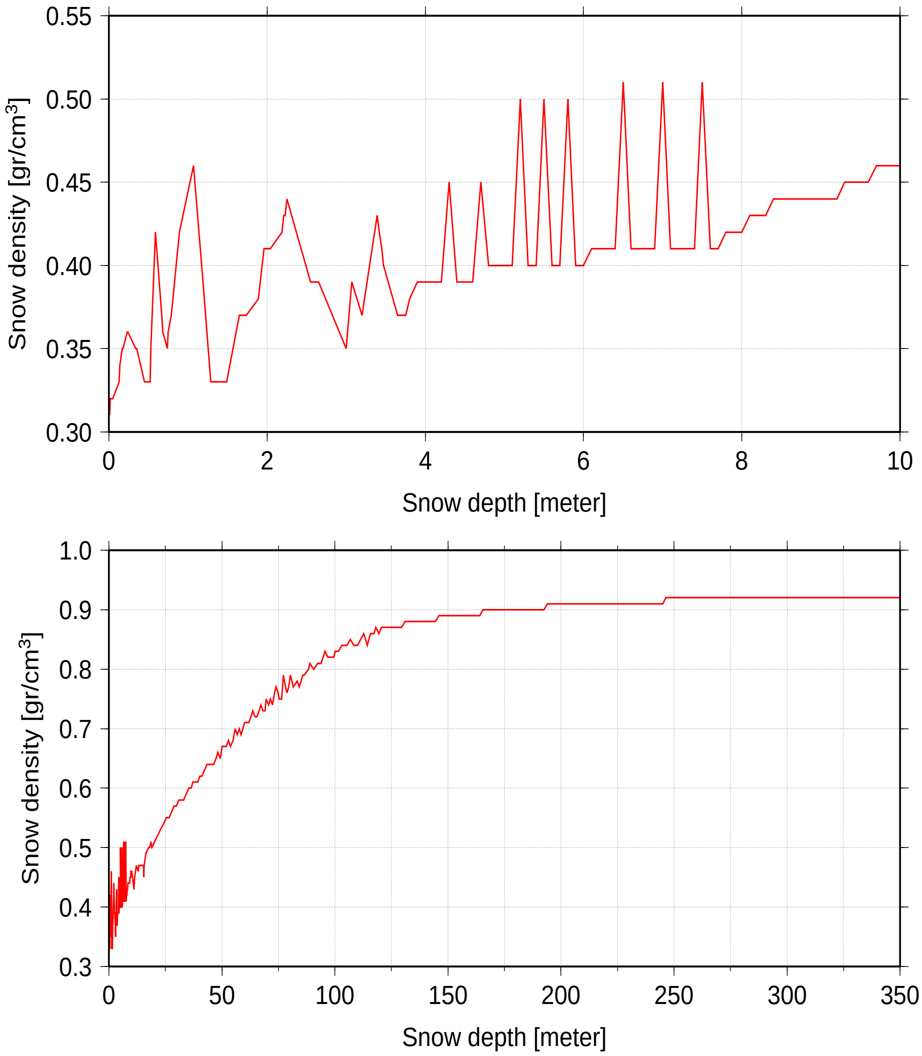

Figure 134.: Snow density of the snow as a function of the depth, as provided by IFAC. [Top] First 10 meters, [Bottom] 350 meters depth.

E.4 RADIOMETRIC MEASUREMENTS FROM DOMEX-2

With the objective of verifying the applicability of the East Antarctic plateau as an extended target for calibrating and monitoring the performances of SMOS, DOMEX-2 experimental campaigns were carried on in Dome-C in 2008-2009 and 2009-2010 by IFAC and other scientific partners. They mainly consisted in brightness temperature measurements in two polarizations (Vertical and Horizontal), taken by the L-band (1413 MHz) RaDomeX radiometer, for evaluating the long-time stability of L-band microwave emission of the snow surface, while passive satellite data (from SMOS itself and AMSR-E in other frequency bands) were envisaged for evaluating the spatial stability.

There were no radiometric measurements during the days of acquisition of GPS reflections. However, the seasonal variability found in the brightness temperature suggests a constant daily pattern (solar-dependent) for the short period considered here. Therefore, there was not an apparent link between the radiometric measurements and the amplitude's fluctuations obtained in the GPS-R observables and introduced in Chapter 3. Fortunately for our research purposes related to sub-surface contributions of the snow layers to the GPS reflections, an unexpected behavior was found in the brightness temperature results of DOMEX-2. For the given geometry of the experimental setup, with the instrument installed 13 m high in the American tower and pointing towards the snow surface with a typical incidence angle of 42° and an Azimuth angle of 315° (North-West), significant peaks in the horizontal component of the brightness temperature (T_h) were detected when a specular reflection of the Sun was entering the main beam of the antenna (with a 3 dB beamwidth of $\sim$30°). An example is displayed in Figure 135. Notice that during this "Sun reflection's interference", the parameter T_h shows a figure with several peaks rather than the smooth pattern that would be obtained by simply assuming a Sun surface reflection entering through the shape of the radiometer's antenna beam. The model developed in Chapter 5 for generating L-band GPS reflections from several dry snow layers has been adapted to this situation, and its analysis and the results obtained are shown in the same Chapter.

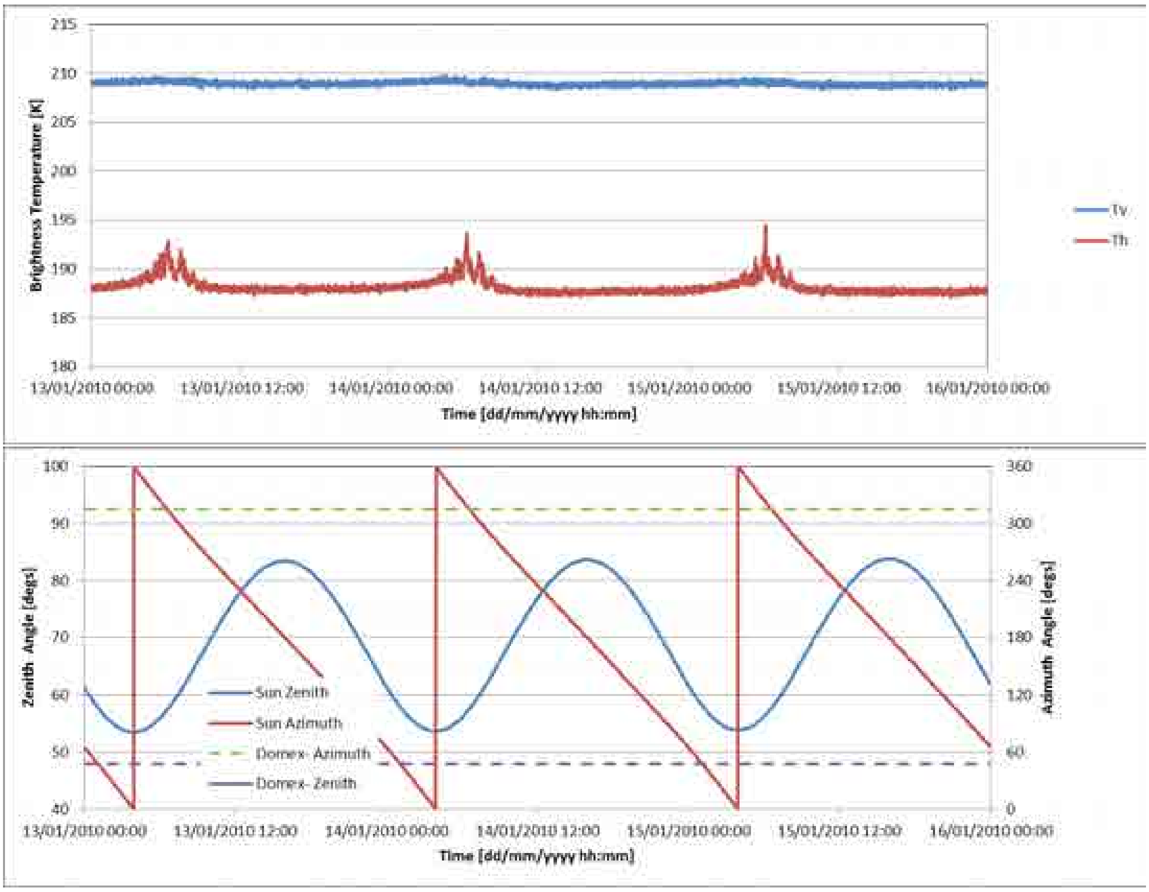

Figure 135.: [Top] Vertical (T_v) and Horizontal (T_h) components of brightness temperature measured during three days of DOMEX-2 experimental campaign (January 13 to 16, 2010). Unexpected periodic fluctuations appear in T_h. [Bottom] Position of the Sun (Azimuth and Zenith –elevation– in solid lines) compared with the radiometer's antenna orientation (dashed lines). The antenna has a 3 dB beamwidth of $\sim 30°$ (symmetric for both E/H planes) in both polarizations. Notice that there is time coincidence between the crossing pass of the Sun into the antenna orientation and the fluctuation events. Plots provided by Giovanni Macelloni (IFAC).

F

COMPUTATION OF THE OFFSET DELAY IN A KINEMATIC SYSTEM

The objective of this Appendix is to present the algorithms used to compute the distance correction $\widehat{\rho_{ant}}$ in a kinematic system (typically an aircraft). This term has to be added (with the obtained sign $\pm$) to the delay of a signal arriving to a secondary antenna, in order to obtain the equivalent delay that the same signal would experience to reach the reference antenna. In our case, the reference antenna is the Up-looking one and the secondary antenna is the one used to gather the reflected signals (Figure 136).

The relative position between the secondary antenna and the reference antenna is given by vector $\vec{b}$. The quantity to compute is the projection of this vector in the arrival direction of the signal reflected at the specular point defined by the corresponding unit vector $\vec{e}$.

In our computations, we use the following two reference frames, centered in the reference antenna:

- $\{xyz\}$ is an aircraft body frame (Figure 137) with 1-axis pointing aircraft forward, 3-axis pointing aircraft down and 2-axis forming a direct system.
- $\{NED\}$ is a local coordinate reference, with the 1-axis pointing towards North, 2-axis pointing towards East and 3-axis pointing downwards.

To transform the coordinates of $\vec{b}$ from $\{x, y, z\}$ to $\{NED\}$ we use the angles produced by the inertial measurement unit: roll (θ_{BF}), pitch (ϕ_{BF}) and yaw (ψ_{BF}), with the sign convention as sketched in Figure 137 using the formula:

$$[b]_{\{NED\}} = Rot_z(\psi_{BF}) \cdot Rot_y(\phi_{BF}) \cdot Rot_x(\theta_{BF}) \cdot [b]_{\{xyz\}} \tag{117}$$

where the rotation matrices are:

$$Rot_x(\theta_{BF}) = \begin{bmatrix} 1 & 0 & 0 \\ 0 & \cos(\theta_{BF}) & -\sin(\theta_{BF}) \\ 0 & \sin(\theta_{BF}) & \cos(\theta_{BF}) \end{bmatrix}$$

$$Rot_y(\phi_{BF}) = \begin{bmatrix} \cos(\phi_{BF}) & 0 & \sin(\phi_{BF}) \\ 0 & 1 & 0 \\ -\sin(\phi_{BF}) & 0 & \cos(\phi_{BF}) \end{bmatrix}$$

$$Rot_z(\psi_{BF}) = \begin{bmatrix} \cos(\psi_{BF}) & -\sin(\psi_{BF}) & 0 \\ \sin(\psi_{BF}) & \cos(\psi_{BF}) & 0 \\ 0 & 0 & 1 \end{bmatrix}$$

Two additional reference frames are used in our algorithms:

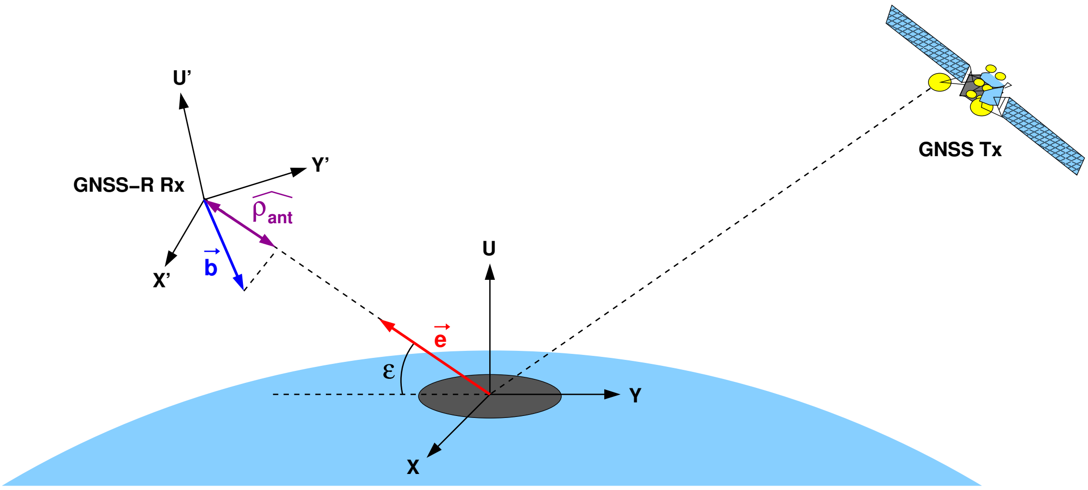

Figure 136.: The offset delay is the projection of the baseline $\vec{b}$ into the direction $\vec{e}$.

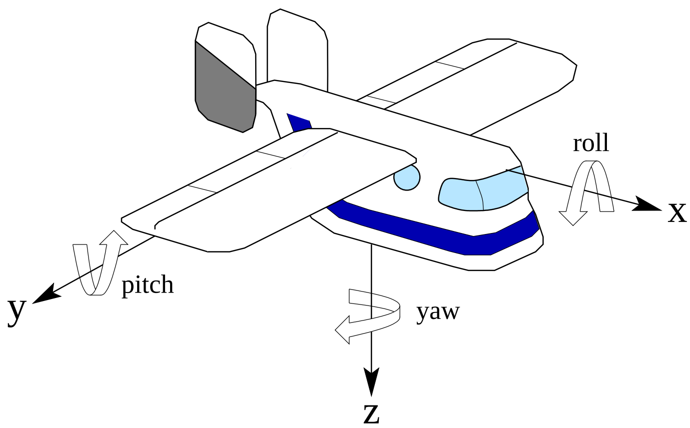

Figure 137.: Aircraft body frame.

- $\{ENU\}$ is a local coordinate reference, with the 1-axis pointing towards East, 2-axis pointing towards North and 3-axis pointing upwards.
- $\{XYU\}$ is a local direct reference frame with the 3-axis pointing upwards and the plane $\{Y, U\}$ contains the transmitter, the receiver and the specular point, with $Y_{transmitter} > 0$.

The transformation of the $\{NED\}$ to the $\{ENU\}$ is accomplished using:

$$[b]_{\{ENU\}} = T_{ENU}^{NED}\,[b]_{\{NED\}} \tag{118}$$

where

$$T_{ENU}^{NED} = \begin{bmatrix} 0 & 1 & 0 \\ 1 & 0 & 0 \\ 0 & 0 & -1 \end{bmatrix}$$

The coordinates of the $\vec{b}$ in the $\{XYU\}$ are computed using the following approximation:

$$[b]_{\{XYU\}} \approx Rot_z(\beta)\,[b]_{\{ENU\}} \tag{119}$$

where β is the local azimuth of the transmitter (clockwise from North) and Rot_z is a rotation around the 3-axis as defined before. Note that we are doing an approximation. Note from Figure 136 that we should have defined an additional local frame $\{X'Y'U'\}$ centered at the reference antenna. However, since in our scenario the receiver will be always close enough to the Earth surface (when comparing to the GPS satellite), we can assume that $[b]_{\{XYU\}} \approx [b]_{\{X'Y'U'\}}$

The unit vector $\vec{e}$ depends, when expressed in the $\{XYU\}$ coordinates, on the local elevation of the transmitter ε:

$$[e]_{\{XYU\}} = \begin{bmatrix} 0 \\ -\cos(\varepsilon) \\ \sin(\varepsilon) \end{bmatrix}$$

Grouping the different elements we can compute $\widehat{\rho_{ant}}$ as the dot product between arrays $[e]_{\{XYU\}}$ and $[b]_{\{XYU\}}$.

G

AVERAGING OF LAG-HOLOGRAMS

G.1 PRN-AVERAGE

We reproduce here three pairs of PRN, each pair covering a similar segment of the elevation/elevation-rate space, and the three pairs located in different areas of such space. Their tracks in elevation/elevation-rate are displayed in Figure 138.

Figure 139 shows the averaged lag-holograms of these pairs, for day December 16 2009. The features of each lag-hologram reassembles those of the paired PRN, while differences are appreciable between different pairs.

Similar comparisons are obtained for the other analyzed days, because the PRN-averaged lag-holograms have a strong repeatability. For completeness, we compile in Figure 140 the daily series for PRN02.

The similitude between the paired PRNs, which cover a similar arch of the elevation-elevation rate space, together with the time repeatability, seems to indicate that the bands in the lag-holograms are indeed stable signals.

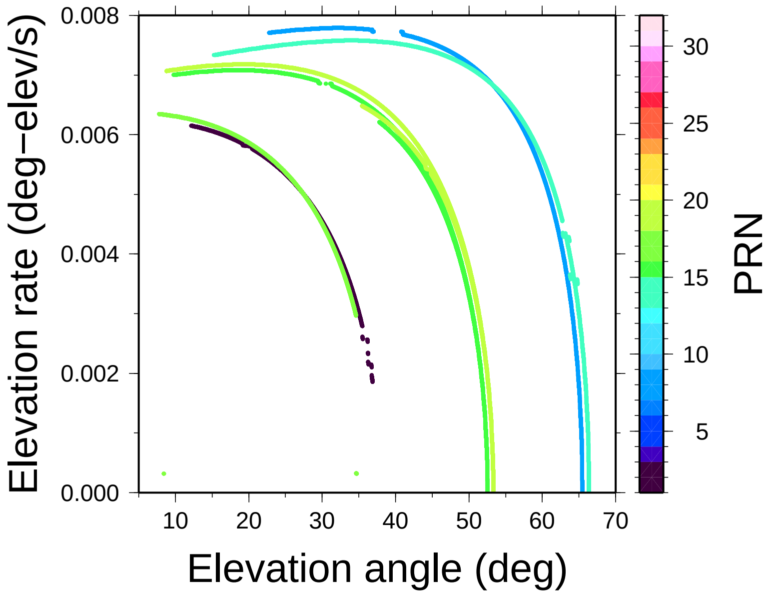

Figure 138.: Elevation/elevation-rate tracks of the three pairs of PRN for which the averaged lag-holograms are analyzed in Figure 139. On the left the pair PRN02 and PRN17, in the center PRN15 and PRN19, and on the right PRN08 and PRN13.

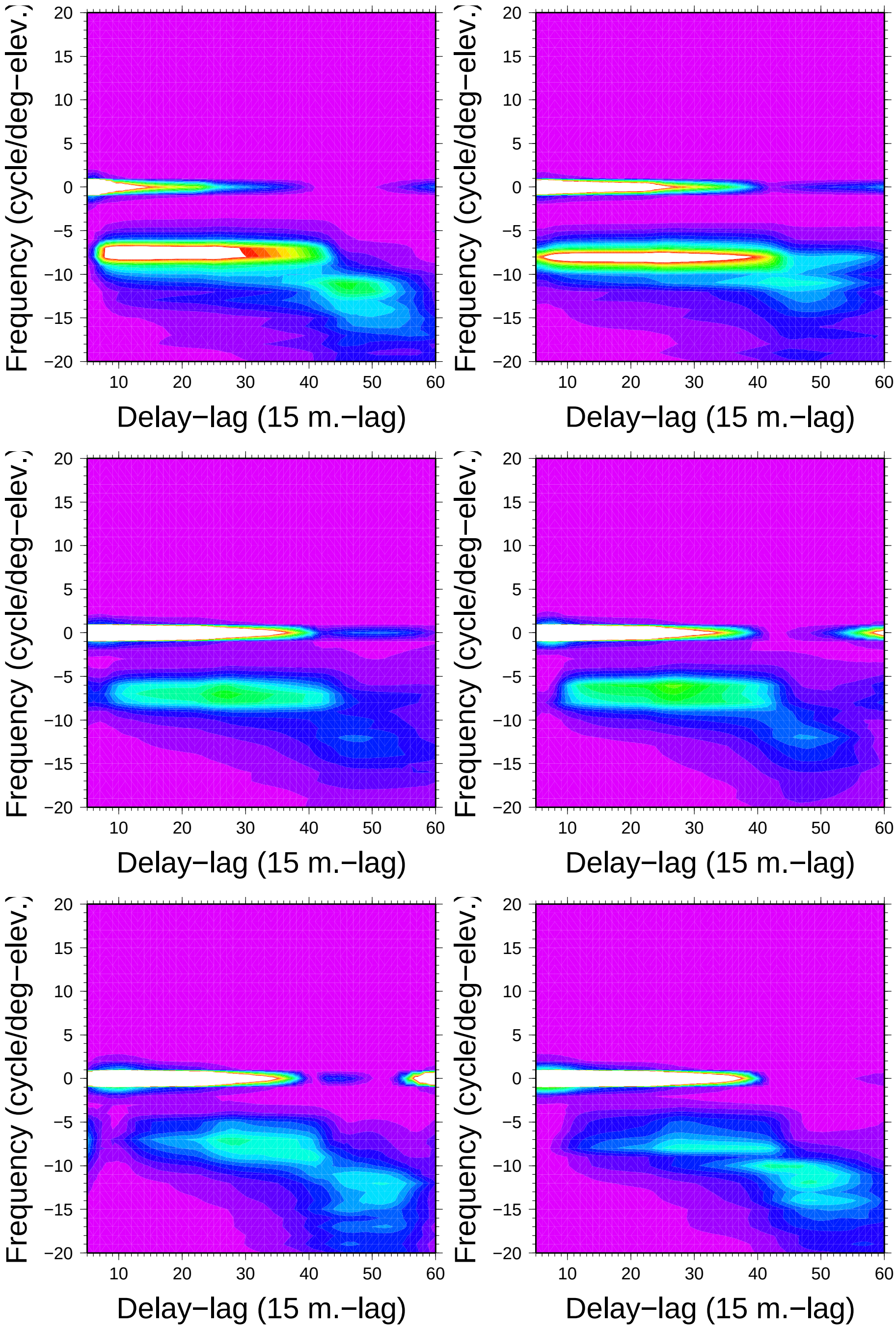

Figure 139.: PRN-averaged lag-holograms for three pairs of PRNs, corresponding to December 16 2009: (top) PRN02 and PRN17; (middle) PRN15 and PRN19; (bottom) PRN08 and PRN13. All use the same color scale (arbitrary units).

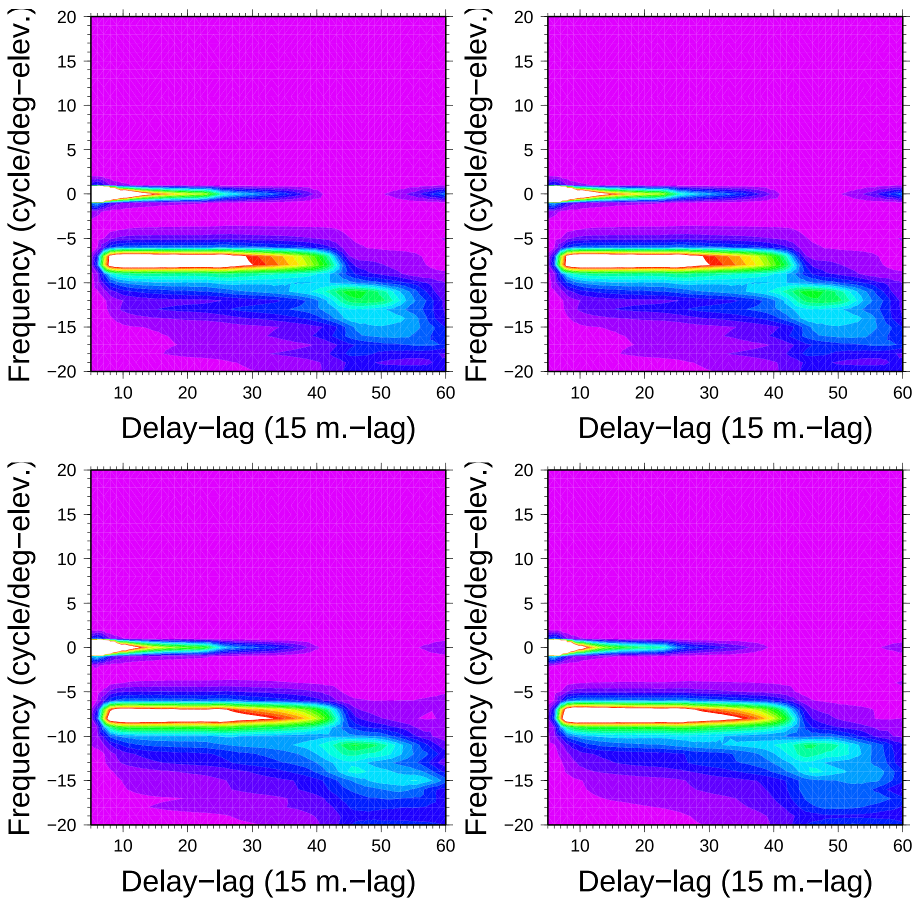

Figure 140.: PRN02-averaged lag-holograms, for days 17 to 20 December 2009. Compare with day December 16 in Figure 139. All have been produced with the same color scale (arbitrary units).

G.2 ELEVATION-AVERAGE

For each day (between 16th and 21st December 2009), all the lag-hologram observations laying within 5°-elevation cells have been averaged. Each cell thus contains the variability associated to 5°-elevation change, plus the diversity of elevation-rates and geographic location of the reflection (different PRNs).

As the elevation angle increases (incidence angle decreases), we observe (in Figure 141):

- The main negative frequency band (zero-frequency band is leakage of direct signal before lag 42, and floor noise continuous component contribution after lag 42) approaches to zero frequency. This is consistent with Figure 78.
- The features are better defined in central elevation angles up to 50°, whereas at higher elevation (lower incidence) most of the reflection features fade away. This is a sign that within the 5°-elevation range of the averaging cell there is more variability at elevations higher than 55° than at lower angles of observation. This is not only related to the range of elevation-rates being observed at that cell, because as shown in Figure 93, the elevation cells with largest range of elevation-rates are between 40° and 50°. There must be other sources of variability of the lag-hologram above 55° elevation.

Similar comparisons are obtained for the other analyzed days, because the elevation-averaged lag-holograms have a strong repeatability. For completeness, we compile in Figure 142 the daily series for the elevation cell centered at 42.5°.

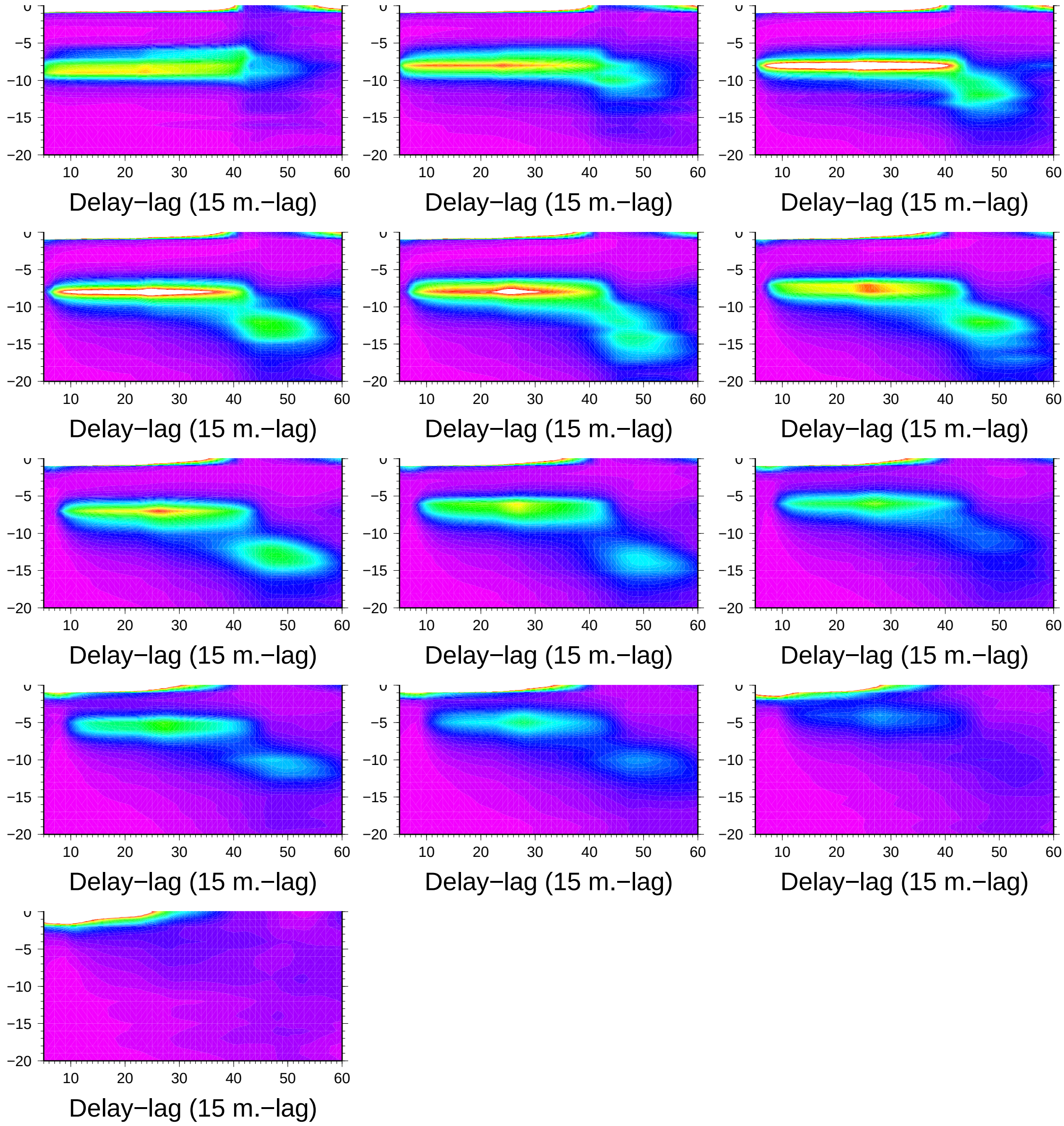

Figure 141.: Elevation-averaged lag-holograms for December 16, 2009. All figures use the same color scale (arbitrary units). The y-axis' variable is frequency in cycles/deg-elev, and they have been cut at 0 to fit all the panels in a single page. Left to right and top to bottom: Elevation rise from 7.5° to 67.5° in steps of 5° (each containing ±2.5°-elevation observations).

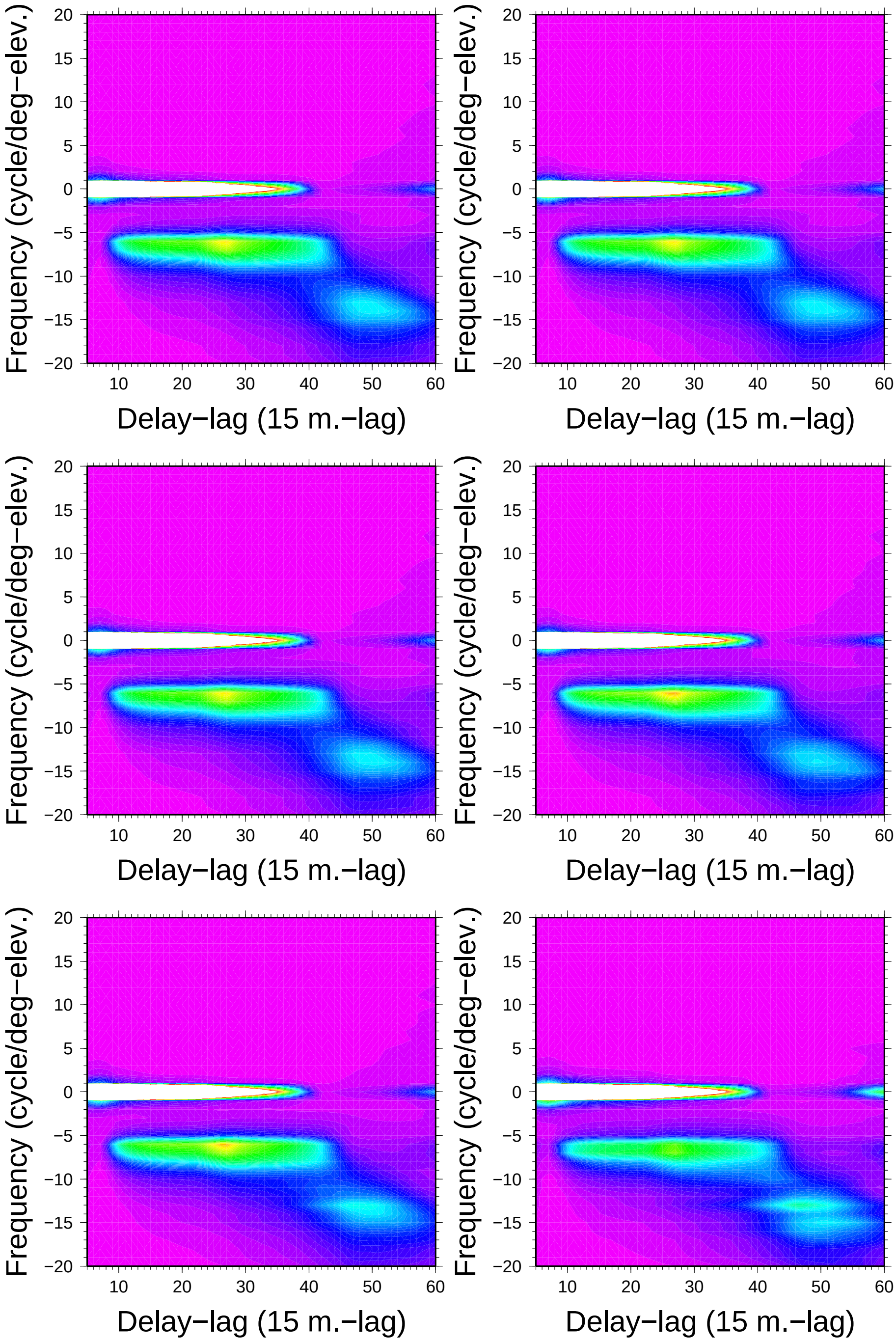

Figure 142.: Repeatability of the elevation-averaged lag-hologram, corresponding to elevation cell centered at 42.5° (±2.5°), December 16 to 21, 2009.

G.3 ELEVATION RATE-AVERAGE

For each day (between 16th and 21st December 2009), all the lag-hologram observations laying within $0.001^\circ/\text{s}$ elevation rate cells have been averaged. Each cell thus contains the variability associated to $0.001^\circ/\text{s}$ rate change, plus the diversity of elevation angles and geographic location of the reflection (different PRNs).

As seen in Figure 143, as the rate decreases the sub-surface contributions tend to fade away. That would associate larger variability within the lag-holograms sharing low rates of elevation than those sharing high rates. However, as shown in Figure 93, high elevation-rate cells contain a wider range of elevation angles, whereas low elevation-rate cells are confined to elevation angles above $\sim 40^\circ$. The higher variability at lower rates, thus, does not come from the diversity of elevation angles. On the contrary, it looks like at higher elevation rates, the lag-hologram are more similar between them, in spite of having being observed at a wider diversity of elevation angles.

Similar comparisons are obtained for the other analyzed days, because the elevation rate-averaged lag-holograms have a strong repeatability. For completeness, we compile in Figure 144 the daily series for the elevation-rate cell centered at $0.0075^\circ/\text{s}$.

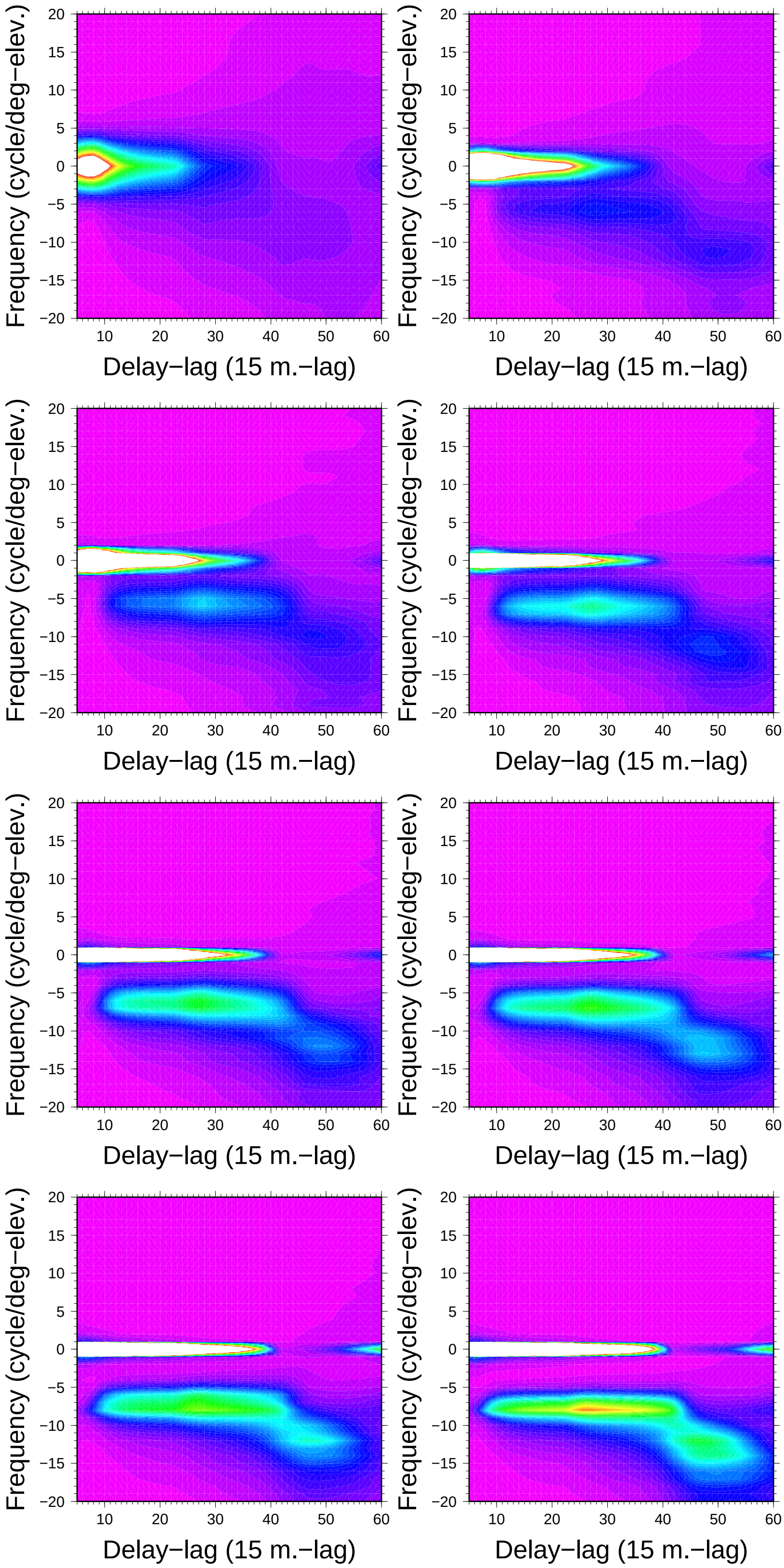

Figure 143.: Elevation rate-averaged lag-holograms for December 16, 2009. All figures use the same color scale (arbitrary units). Elevation rate rise from 0.0005 to 0.0075°/s in steps of 0.001°/s (each containing ±0.0005°/s elevation rate observations) (left to right and top to bottom).

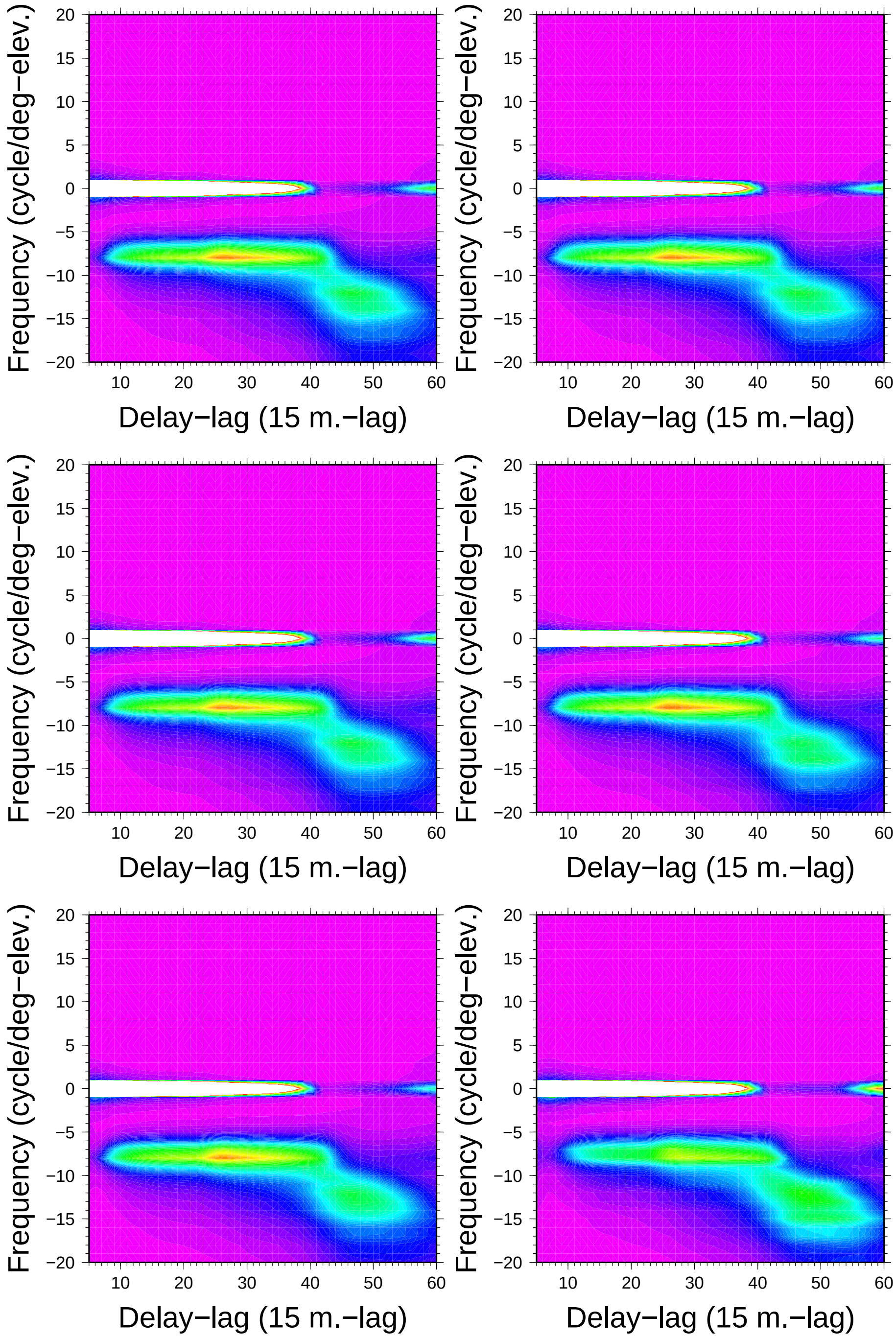

Figure 144.: Repeatability of the elevation rate-averaged lag-hologram, corresponding to elevation-rate cell centered at 0.0075°/s (±0.0005°/s), December 16 to 21, 2009.

BIBLIOGRAPHY

Amarouche, L., Thibaut, P., Zanife, O. Z., Dumont, J. P., Vincent, P., and Steunou, N. (2004). Improving the Jason-1 Ground Retracking to Better Account for Attitude Effects. *Marine Geodesy*, (27):171–198.

Amlien, J. (2008). Remote sensing of snow with passive microwave radiometers - A review of current algorithms. Technical Report Report No 1019, Norsk Regnesentral / Norwegian Computing Center.

Andersen, S., Tonboe, R., Kaleschke, L., Heygster, G., and Pedersen, L. T. (2006). Intercomparison of passive microwave sea ice concentration retrievals over the high concentration Arctic sea ice. *Journal of Geophysical Research*.

Anderson, H. S. and Long, D. G. (2005). Sea ice mapping method for SeaWinds. *IEEE Transactions on Geoscience and Remote Sensing*, 43(3):647–657.

Apel, J. R. (1994). An improved model of the ocean surface wave vector spectrum and its effects on radar backscatter. *Journal of Geophysical Research*, 99(C8).

BeiDou (2013). BeiDou Navigation Satellite System (Development plan). http://en.beidou.gov.cn/introduction.html.

Belmonte, M., Maslanik, J. A., and Axelrad, P. (2009). Bistatic scattering of GPS signals off Arctic sea ice. *IEEE Transactions on Geoscience and Remote Sensing*, 48.

Belmonte-Rivas, M. (2007). *Bistatic Scattering of Global Positioning System Signals from Arctic Sea Ice*. PhD thesis, University of Colorado.

Belmonte-Rivas, M. and Stoffelen, A. (2011). New Bayesian Algorithm for Sea Ice Detection With QuikSCAT. *IEEE Transactions on Geoscience and Remote Sensing*, 49(6):1894–1901.

Burns, B. A., Schmidt-Gröttrup, M., and Viehoff, T. (1992). Methods for digital analysis of AVHRR sea ice images. *IEEE Transactions on Geoscience and Remote Sensing*, 30(3):589–602.

Byun, S. H., Hajj, G. A., and Young, L. E. (2002). Development and application of GPS signal multipath simulator. *Radio Science*, 37(6).

Cardellach, E. (2002). *Sea Surface Determination Using GNSS Reflected Signals*. PhD thesis, Univ. Politècnica de Catalunya (UPC)/ Institut d'Estudis Espacials de Catalunya (IEEC), Barcelona, Spain.

Cardellach, E., Ao, C. O., de la Torre Juárez, M., and Hajj, G. A. (2004). Carrier phase delay altimetry with GPS-reflection/ocultation interferometry from low Earth orbiters. *Geophysical Research Letters*, 31.

Cardellach, E., Fabra, F., Nogués-Correig, O., Oliveras, S., Ribó, S., and Rius, A. (2011). GNSS-R ground-based and airborne campaigns for Ocean, Land, Ice and Snow techniques: application to the GOLD-RTR datasets. *Radio Science*, 46(RS0C04).

Cardellach, E., Fabra, F., Rius, A., Pettinato, S., and D'Addio, S. (2012). Characterization of Dry-snow Sub-structure using GNSS Reflected Signals. *Remote Sensing of Environment*, 124:122–134.

Cardellach, E., Ribó, S., and Rius, A. (2006). Technical Note on POlarimetric Phase Interferometry (POPI). *Arxiv preprint physics/0606099*.

Cardellach, E., Ruffini, G., Pino, D., Rius, A., Komjathy, A., and Garrison, J. L. (2003). Mediterranean Balloon Experiment: ocean wind speed sensing from the stratosphere using GPS reflections. *Remote Sensing of Environment*, 88(3):351–362.

Cavalieri, D. J., Parkinson, C. L., Gloersen, P., Comiso, J. C., and Zwally, H. J. (1999). Deriving long-term time series of sea ice cover from satellite passive-microwave multisensor data sets. *Journal of Geophysical Research*, 104:15803–15814.

Clarizia, M., Gommenginger, C., Bisceglie, M. D., Galdi, C., and Srokosz, M. A. (2012). Simulation of L-Band Bistatic Returns From the Ocean Surface: A Facet Approach With Application to Ocean GNSS Reflectometry. *IEEE Transactions on Geoscience and Remote Sensing*, 50(3):960–971.

Colbeck, S. C., Akitaya, E., Armstrong, R., Gubler, H., Lafeuille, J., Lied, K., McClung, D., and Morris, E. (1990). The international classification for seasonal snow on the ground. Technical report, International Commission of Snow and Ice, IAHS.

Comiso, J. C., Cavalieri, D. J., and Markus, T. (2003). Sea ice concentration, ice temperature, and snow depth using AMSR-E data. *IEEE Transactions on Geoscience and Remote Sensing*, 41(2):243–252.

Comiso, J. C., Parkinson, C. L., Gersten, R., and Stock, L. (2008). Accelerated decline in the Arctic sea ice cover. *Geophysical Research Letters*, 35.

Dedrick, K. R., Partington, K., Woert, M. V., Bertoia, C. A., and Benner, D. (2001). U. S. National/Naval Ice Center Digital Sea Ice Data and Climatology. *Canadian Journal of Remote Sensing/Journal Canadien de Teledetection*, 27(5):457–475.

Drinkwater, M. R., Long, D. G., and Bingham, A. W. (2001). Greenland snow accumulation estimates from satellite radar scatterometer data. *Journal of Geophysical Research*, 106:33935–33950.

Drüe, C. and Heinemann, G. (2004). High-resolution maps of the sea-ice concentration from MODIS satellite data. *Geophysical Research Letters*, 31.

Dunbar, R. S., Lungu, T., Weiss, B., Stiles, B., Huddleston, J., Callahan, P. S., Shirtliffe, G., Perry, K. L., Hsu, C., Mears, C., Wentz, F., and Smith, D. (2006). QuikSCAT Science Data Product User Manual. JPL Document D-18053 - Rev A.

EC (2013). European Comission. Galileo : Satellite launches. http://ec.europa.eu/enterprise/policies/satnav/galileo/satellite-launches.

Eisen, O., Frezzotti, M., Genthon, C., Isaksson, E., Magand, O., van den Broeke, M. R., Dixon, D. A., Ekaykin, A., Holmlund, P., Kameda, T., Karlöf, L., Kaspari, S., Lipenkov, V. Y., Oerter, H., Takahashi, S., and Vaughan, D. G. (2008). Ground-based measurements of spatial and temporal variability of snow accumulation in East Antarctica. *Reviews of Geophysics*, 46:1–39.

Elfouhaily, T., Chapron, B., Katsaros, K., and Vandemark, D. (1997). A unified directional spectrum for long and short wind-driven waves. *Journal of Geophysical Research*, 102(C7):15781–15796.

Elósegui, P., Davis, J. L., Jaldehag, T. K., Johansson, J. M., Niell, A. E., and Shapiro, I. I. (1995). Geodesy using the Global Positioning System: The effects of signal scattering on estimates of site position. *Journal of Geophysical Research*, 100(B7):9921–9934.

EPICA (2004). Eight glacial cycles from an Antarctic ice core. *Nature*, 429:623–628. EPICA community members.

Eppler, D. T., Farmer, L. D., Lohanick, A. W., Anderson, M. R., Cavalieri, D. J., Comiso, J., Gloersen, P., Garrity, C., Grenfell, T. C., Hallikainen, M., Maslanik, J. A., Mätzler, C., Melloh, R. A., Rubinstein, I., and Swift, C. T. (1992). Passive Microwave Signatures of Sea Ice. In Carsey, F. D., editor, *Microwave Remote Sensing of Sea Ice*, chapter 4, pages 47–72. American Geophysical Union, Washington DC, USA.

ESA (2013). Galileo Navigation (Next steps). http://www.esa.int/Our_Activities/Navigation/The_future_-_Galileo/Next_steps.

Fabra, F., Cardellach, E., Nogués-Correig, O., Oliveras, S., Ribó, S., Rius, A., Belmonte, M., Semmling, M., Macelloni, G., Pettinato, S., Zasso, R., and D'Addio, S. (2010). Monitoring sea ice and dry snow with GNSS reflections. In *Proceedings IEEE IGARSS*, pages 3837 – 3840, Honolulu, HI, USA. IEEE Geoscience and Remote Sensing Society.

Fabra, F., Cardellach, E., Nogués-Correig, O., Oliveras, S., Ribó, S., Rius, A., and Belmonte-Rivas, M. (2009). Sea Ice remote sensing with GNSS Reflections. In *Instrumentation Viewpoint ISSN 1886-4864*.

Fabra, F., Cardellach, E., Nogués-Correig, O., Oliveras, S., Ribó, S., Rius, A., Macelloni, G., Pettinato, S., and D'Addio, S. (2011a). An empirical approach towards characterization of dry snow layers using GNSS-R. In *Proceedings IEEE IGARSS*, pages 4379 – 4382, Vancouver, BC, Canada. IEEE Geoscience and Remote Sensing Society.

Fabra, F., Cardellach, E., Rius, A., Ribó, S., Oliveras, S., Nogués-Correig, O., Belmonte-Rivas, M., Semmling, M., and D'Addio, S. (2011b). Phase Altimetry with Dual Polarization GNSS-R over Sea Ice. *IEEE Transactions on Geoscience and Remote Sensing*, 50(6):10.

Fabra, F., Cardellach, E., Rius, A., Ribó, S., Oliveras, S., Nogués-Correig, O., Macelloni, G., Pettinato, S., and D'Addio, S. (2011c). GNSS-R for the Retrieval of Internal Layers' Information from Dry Snow Masses. In *Proceedings of 3rd International Colloquium - Scientific and Fundamental Aspects of the Galileo Programme*. European Space Agency.

Fabra, F., Cardellach, E., Rius, A., Ribó, S., Oliveras, S., Nogués-Correig, O., Semmling, M., Macelloni, G., Pettinato, S., Belmonte-Rivas, M., and D'Addio, S. (2011d). GNSS Reflectometry for the remote sensing of sea ice and dry snow. In *Proceedings of the third Workshop on Advanced RF Sensors and Remote Sensing Instruments*. European Space Agency.

Fassnacht, S. R., Williams, M. W., and Corrao, M. V. (2009). Changes in the surface roughness of snow from millimetre to metre scales. *Ecological Complexity*, 9:221–229.

Fetterer, F. M., Drinkwater, M. R., Jezek, K. C., Laxon, S. W. C., Onstott, R. G., and Ulander, L. M. H. (1992). Sea Ice Altimetry. In Carsey, F. D., editor, *Microwave Remote Sensing of Sea Ice*, chapter 7, pages 111–135. American Geophysical Union, Washington DC, USA.

Friis, H. T. (1944). Noise Figures of Radio Receivers. *Proceedings of the IRE*, 32(7):419–422.

Fung, A. K. (1994). *Microwave Scattering and Emission Models and Their Applications*. Artech House, Inc.

Garrison, J. L., Komjathy, A., Zavorotny, V. U., and Katzberg, S. J. (2002). Wind Speed Measurement Using Forward Scattered GPS Signals. *IEEE Transactions on Geoscience and Remote Sensing*, 40(1):50–65.

GCOS (2009). Guideline for the Generation of Satellite-based Datasets and Products meeting GCOS Requirements. GCOS-128 (WMO/TD No. 1488).

Gleason, S. (2005). Detection and processing of bistatically reflected GPS signals from low earth orbit for the purpose of ocean remote sensing. *IEEE Transactions on Geoscience and Remote Sensing*, 43.

Gleason, S. (2010). Towards Sea Ice Remote Sensing with Space Detected GPS Signals: Demonstration of Technical Feasibility and Initial Consistency Check Using Low Resolution Sea Ice Information. *Remote Sensing*, pages 2017–2039.

Hajj, G. and Zuffada, C. (2003). Theoretical description of a bistatic system for ocean altimetry using the GPS signal. *Radio Science*, 38(5):1089–2008.

Hall, D. K., Key, J. R., Casey, K. A., Riggs, G. A., and Cavalieri, D. (2004). Sea Ice Surface Temperature Product From MODIS. *IEEE Transactions on Geoscience and Remote Sensing*, 42:5.

Hall, D. K., Riggs, G. A., and Salomonson, V. V. (2009). *MODIS/Aqua Sea Ice Extent 5-Min L2 Swath 1km V005*. 2009, updated daily. January to May 2009. Boulder, Colorado USA: National Snow and Ice Data Center. Digital media.

Hall, D. K., Riggs, G. A., Salomonson, V. V., DiGirolamo, N. E., and Bayr, K. J. (2002). MODIS snow-cover products. *Remote Sensing of Environment*, 83:181–194.

Hallikainen, M. and Winebrenner, D. P. (1992). The Physical Basis for Sea Ice Remote Sensing. In Carsey, F. D., editor, *Microwave Remote Sensing of Sea Ice*, chapter 3, pages 29–46. American Geophysical Union, Washington DC, USA.

Hawley, R. L., Morris, E. M., Cullen, R., Nixdorf, U., Shepherd, A. P., and Wingham, D. J. (2006). ASIRAS airborne radar resolves internal annual layers in the dry-snow zone of Greenland. *Geophysical Research Letters*, 33.

Helm, A., Montenbruck, O., Ashjaee, J., Yudanov, S., Beyerle, G., Stosius, R., and Rothacher, M. (2007). GORS - a GNSS occultation, reflectometry and scatterometry space receiver. In *ION-GNSS-2007 Conference*, Fort Worth, Texas, USA.

IERS (2003). *IERS Technical Note No. 32*. IERS Central Bureau, Frankfurt am Main, Germany.

Igarashi, K., Pavelyev, A., Hocke, K., Pavelyev, D., Kucherjavenkov, I. A., Matyugov, S., Zakharov, A., and Yakovlev, O. (2000). Radio holographic principle for observing natural processes in the atmosphere and retrieving meteorological parameters from radio occultation data. *Earth Planets and Space*, 52(11):893–899.

IGS (2013). The International GNSS Service (IGS). http://igscb.jpl.nasa.gov/.

Jacobson, M. D. (2010). Inferring Snow Water Equivalent for a Snow-Covered Ground Reflector Using GPS Multipath Signals. *Remote Sensing*, 2:2426–2441.

Kaleschke, L., Tian-Kunze, X., Mäkynen, N. M. M., and Drusch, M. (2012). Sea ice thickness retrieval from SMOS brightness temperatures during the Arctic freeze-up period. *Geophysical Research Letters*, 39.

Katzberg, S. J., Torres, O., Grant, M. S., and Masters, D. (2006). Utilizing calibrated GPS reflected signals to estimate soil reflectivity and dielectric constant: Results from SMEX02. *Remote Sensing of Environment*, 100(1):17–28.

Key, J. and Haefliger, M. (1992). Arctic ice surface temperature retrieval from AVHRR thermal channels. *Journal of Geophysical Research*, 97(D5):5885–5893.

Komjathy, A., Maslanik, J., Zavorotny, V. U., Axelrad, P., and Katzberg, S. J. (2000a). Sea Ice Remote Sensing Using Surface Reflected GPS Signals. In *Proceedings IEEE IGARSS*, pages 2855–2857, Honolulu, HI, USA.

Komjathy, A., Zavorotny, V. U., Axelrad, P., Born, G. H., and Garrison, J. L. (2000b). GPS signal scattering from sea surface: Wind-speed retrieval using experimental data and theoretical model. *Remote Sensing of Environment*, 73(2):162–174.

Koskinen, J. T., Pulliainen, J. T., and Hallikainen, M. T. (1997). The Use of ERS-1 SAR Data in Snow Melt Monitoring. *IEEE Transactions on Geoscience and Remote Sensing*, 35(3):601–610.

Kwok, R. (2002). Sea ice concentration estimates from satellite passive microwave radiometry and openings from SAR ice motion. *Geophysical Research Letters*, 29(9).

Lacroix, P., Dechambre, M., Legrésy, B., Blarel, F., and Rémy, F. (2008a). On the use of the dual-frequency ENVISAT altimeter to determine snowpack properties of the Antarctic ice sheet. *Remote Sensing of Environment*, 112:1712–1729.

Lacroix, P., Legrésy, B., Langley, K., Hamran, S., Kohler, J., Roques, S., Rémy, F., and Dechambre, M. (2008b). In situ measurements of snow surface roughness using a laser profiler. *Journal of Glaciology*, 54(187):753–762.

Larson, K. M., Gutmann, E., Zavorotny, V., Braun, J., Williams, M., and Nievinski, F. (2009). Can we measure snow depth with GPS receivers? *Geophysical Research Letters*, 36.

Lemke, P., Ren, J., Alley, R. B., Allison, I., Carrasco, J., Flato, G., Fujii, Y., Kaser, G., Mote, P., Thomas, R. H., and Zhang, T. (2007). Observations: Changes in Snow, Ice and Frozen Ground. In Solomon, S., Qin, D., Manning, M., Chen, Z., Marquis, M., Averyt, K. B., Tignor, M., and Miller, H. L., editors, *Climate Change 2007: The Physical Science Basis. Contribution of Working Group I to the Fourth Assessment Report of the Intergovernmental Panel on Climate Change*, chapter 4, pages 337–383. Cambridge University Press, Cambridge, United Kingdom and New York, NY, USA.

Lowe, S. T., LaBrecque, J. L., Zuffada, C., Romans, L. J., Young, L. E., and Hajj, G. A. (2002a). First spaceborne observation of an Earth-reflected GPS signal. *Radio Science*, 37(1):1–28.

Lowe, S. T., Zuffada, C., Chao, Y., Kroger, P., Young, L. E., and LaBrecque, J. L. (2002b). 5-cm Precision Aircraft Ocean Altimetry Using GPS Reflections. *Geophysical Research Letters*, 29(10, 1375).

Lyapustin, A., Tedesco, M., Wang, Y., Aoki, T., Hori, M., and Kokhanovsky, A. (2009). Retrieval of snow grain size over Greenland from MODIS. *Remote Sensing of Environment*, 113:1976–1987.

Macelloni, G., Brogioni, M., Crepaz, A., Drinkwater, M. R., and Zaccaria, J. (2009). DOMEX-2 : L-band microwave emission measurements of the Antarctic Plateau. In *Proceedings IEEE IGARSS*, volume 2, pages 1016–1019, Cape Town, South Africa.

Macelloni, G., Brogioni, M., Pampaloni, P., and Cagnati, A. (2007). Multifrequency microwave emission from the Dome-C area on the east antarctic plateau: Temporal and spatial variability. *IEEE Transactions on Geoscience and Remote Sensing*, 45(7):2029–2039.

Macelloni, G., Brogioni, M., Pampaloni, P., Cagnati, A., and Drinkwater, M. R. (2006). DOMEX 2004: An Experimental Campaign at Dome-C Antarctica for the Calibration of Spaceborne Low-Frequency Microwave Radiometers. *IEEE Transactions on Geoscience and Remote Sensing*, 44(10):2642–2653.

Markus, T., Cavalieri, D. J., Gasiewski, A. J., Klein, M., Maslanik, J. A., Powell, D. C., Stankov, B. B., Stroeve, J., and Sturm, M. (2006). Microwave Signatures of Snow on Sea Ice: Observations. *IEEE Transactions on Geoscience and Remote Sensing*, 44(11):3081–3090.

Martín-Neira, M. (1993). A passive reflectometry and interferometry system (PARIS): application to ocean altimetry. *ESA Journal*, 17:331–355.

Martín-Neira, M., D'Addio, S., Buck, C., Floury, N., and Prieto-Cerdeira, R. (2011). The Paris Ocean Altimeter In-orbit Demonstrator. *IEEE Transactions on Geoscience and Remote Sensing*, 49(6):1–29.

Masters, D., Zavorotny, V. U., Katzberg, S. J., and Emery, W. (2000). GPS Signal Scattering from Land for Moisture Content Determination. In *Proceedings IEEE IGARSS*, pages 3090–3092, Honolulu, HI, USA.

Maus, S., Green, C. M., and Fairhead, J. D. (1998). Improved Ocean-geoid Resolution from Retracked ERS-1 Satellite Altimeter Waveforms. *Geophysical Journal International*, 134:243–253.

Misra, P. and Enge, P. (2006). *Global Positioning Systems. Signals, Measurements and Performance*. Ganga-Jamuna Press. ISBN: 0-9709544-1-7.

Mouginot, J., Scheuchl, B., and Rignot, E. (2012). Mapping of Ice Motion in Antarctica Using Synthetic-Aperture Radar Data. *Remote Sensing*, 4:2753–2767.

Nagler, T. and Rott, H. (2000). Retrieval of Wet Snow by Means of Multitemporal SAR Data. *IEEE Transactions on Geoscience and Remote Sensing*, 38(2):754–765.

NASA (2013). Reverb server. http://reverb.echo.nasa.gov/reverb.

Niell, A. (1996). Global mapping functions for the atmospheric delay at radio wavelengths. *Journal of Geophysical Research*, pages 3227–3246.

Nogués-Correig, O., Cardellach Galí, E., Sanz Campderròs, J., and Rius, A. (2007). A GPS-Reflections Receiver That Computes Doppler/Delay Maps in Real Time. *IEEE Transactions on Geoscience and Remote Sensing*, 45(1):156–174.

North, D. O. (1963). An Analysis of the Factors Which Determine Signal/Noise Discrimination in Pulsed Carrier Systems. *Proceedings of the IEEE*, 51(7):1016–1027.

NSIDC (2010). National Ice Center Arctic Sea Ice Charts and Climatologies in Gridded Format. http://nsidc.org/data/docs/noaa/g02172_nic_charts_climo_grid/index.

Ochilov, S. and Clausi, D. A. (2012). Operational SAR Sea-Ice Image Classification. *IEEE Transactions on Geoscience and Remote Sensing*, 50(11):4397–4408.

Onstott, R. G. (1989). Active microwave classification of sea ice. In *Proceedings IEEE IGARSS*, pages 369–374, Vancouver, BC, Canada.

Onstott, R. G. (1992). SAR and Scatterometer Signatures of Sea Ice. In Carsey, F. D., editor, *Microwave Remote Sensing of Sea Ice*, chapter 5, pages 73–104. American Geophysical Union, Washington DC, USA.

Onstott, R. G. and Shuchman, R. A. (2004). SAR Measurements of Sea Ice. In Jackson, C. R. and Apel, J. R., editors, *Synthetic Aperture Radar Marine User's Manual*, chapter 3, pages 81–115. NOAA/NESDIS Office of Research and Applications, Washington DC, USA.

Padman, L. and Erofeeva, S. (2004). A barotropic inverse tidal model for the Arctic Ocean. *Geophysical Research Letters*, 31.

Partington, K. C., Flach, J. D., Barber, D., Isleifson, D., Meadows, P. J., and Verlaan, P. (2010). Dual-Polarization C-Band Radar Observations of Sea Ice in the Amundsen Gulf. *IEEE Transactions on Geoscience and Remote Sensing*, 48(6):2685–2691.

Petit, J. R., Jouzel, J., Pourchet, M., and Merlivat, L. (1982). A Detailed Study of Snow Accumulation and Stable Isotope Content in Dome C (Antarctica). *Geophysical Research Letters*, 87(C6):4301–4308.

PNRA (2013). Meteo-climatological Observatory from Italian Antarctic Research Programme. http://www.climantartide.it/.

Press, W. H., Teukolsky, S. A., Vetterling, W. T., and Flannery, B. P. (2007). *Numerical Recipes: The Art of Scientific Computing, Third Edition*. Cambridge University Press.

PV-DMI (2013). Polar View at DMI. http://ocean.dmi.dk/polarview/.

Remund, Q. P. and Long, D. G. (1999). Sea ice extent mapping using Ku band scatterometer data. *Journal of Geophysical Research*, 104:11515–11528.

Rémy, F. and Parouty, S. (2009). Antarctic Ice Sheet and Radar Altimetry: A Review. *Remote Sensing*, 1:1212–1239.

Rignot, E., Jezek, K. C., and Sohn, H. G. (1995). Ice flow dynamics of the Greenland Ice Sheet from SAR interferometry. *Geophysical Research Letters*, 22(5):575–578.

Rius, A., Aparicio, J. M., Cardellach, E., Martín-Neira, M., and Chapron, B. (2002). Sea surface state measured using GPS reflected signals. *Geophysical Research Letters*, 29(23).

Rius, A., Cardellach, E., and Martín-Neira, M. (2010). Altimetric Analysis of the Sea-Surface GPS-Reflected Signals. *IEEE Transactions on Geoscience and Remote Sensing*, 48(4):2119–2127.

Rodriguez-Alvarez, N., Aguasca, A., Valencia, E., Bosch-Lluis, X., Ramos-Perez, I., Park, H., Camps, A., and Vall-llossera, M. (2011). Snow Monitoring Using GNSS-R Techniques. In *Proceedings IEEE IGARSS*, pages 4375–4378, Vancouver, BC, Canada.

Rosenqvist, A., Shimada, M., Ito, N., and Watanabe, M. (2007). ALOS PALSAR: A Pathfinder mission for global-scale monitoring of the environment. *IEEE Transactions on Geoscience and Remote Sensing*, 47:3307–3316.

Semmling, M., Beyerle, G., Stosius, R., Dick, G., Wickert, J., Fabra, F., Cardellach, E., Ribó, S., Rius, A., Helm, A., Yudanov, S., and D'Addio, S. (2011). Detection of arctic ocean tides using interferometric gnss-r signals. *Geophysical Research Letters*.

Semmling, M., Schmidt, T., Wickert, J., Schön, S., Fabra, F., Cardellach, E., and Rius, A. (2012). On the retrieval of the specular reflection in gnss carrier observations for ocean altimetry. *Radio Science*. in press.

Shepherd, A., Wingham, D., and Rignot, E. (2004). Warm ocean is eroding West Antarctica Ice Sheet. *Geophysical Research Letters*, 31.

Shuchman, R. A., Onstott, R. G., Johannessen, O. M., Sandven, S., and Johannessen, J. A. (2004). Processes at the Ice Edge - The Arctic. In Jackson, C. R. and Apel, J. R., editors, *Synthetic Aperture Radar Marine User's Manual*, chapter 18, pages 373–395. NOAA/NESDIS Office of Research and Applications, Washington DC, USA.

Sihvola, A. and Tiuri, M. (1986). Snow Fork for Field Determination of the Density and Wetness Profiles of a Snow Pack. *IEEE Transactions on Geoscience and Remote Sensing*, GE-24(5):717–721.

Six, D., Fily, M., Alvain, S., Henry, P., and Benoist, J. P. (2004). Surface characterisation of the Dome Concordia area (Antarctica) as a potential satellite calibration site, using Spot 4/Vegetation instrument. *Remote Sensing of Environment*, 89(1):83–94.

Solheim, F. S., Vivekanandan, J., Ware, R. H., and Rocken, C. (1999). Propagation delays induced in GPS signals by dry air, water vapor, hydrometeors, and other particulates. *Journal of Geophysical Research*, 104(D8):9663–9670.

Solomon, S., Qin, D., Manning, M., Chen, Z., Marquis, M., Averyt, K. B., Tignor, M., and Miller, H. L. (2007). *Climate Change 2007: The Physical Science Basis. Contribution of Working Group I to the Fourth Assessment Report of the Intergovernmental Panel on Climate Change*. Cambridge University Press, Cambridge, United Kingdom and New York, NY, USA.

Spilker, J. J., Parkinson, B. W., Axelrad, P., and Enge, P. (1996). *Global Positioning System: Theory and Applications*. Amer. Inst. Aeronaut. Astronaut., Washington, DC.

Stitt, S., Dwyer, J. L., Dye, D. G., and Josberger, E. G. (2011). Terrestrial essential climate variables at a glance. U.S. Geological Survey Scientific Investigations Map 2011-3155, 1 plate.

Stroeve, J. C., Serreze, M. C., Fetterer, F., Arbetter, T., Meier, W., Maslanik, J., and Knowles, K. (2005). Tracking the Arctic's shrinking ice cover: another extreme September minimum in 2004. *Geophysical Research Letters*, 32.

SVN (2011). Apache Subversion (SVN). http://subversion.apache.org.

Treuhaft, R. N., Lowe, S. T., Zuffada, C., and Chao, Y. (2001). Two-cm GPS altimetry over Crater Lake. *Geophysical Research Letters*, 28:4343–4346.

Tucker, W. B., Perovich, D. K., Gow, A. J., Weeks, W. F., and Drinkwater, M. R. (1992). Physical Properties of Sea Ice Relevant to Remote Sensing. In Carsey, F. D., editor, *Microwave Remote Sensing of Sea Ice*, chapter 2, pages 9–28. American Geophysical Union, Washington DC, USA.

Ulaby, F. T., Moore, R. K., and Fung, A. K. (1990a). *Microwave Remote Sensing Active and Passive*, volume III. Artech House, Inc.

Ulaby, F. T., Moore, R. K., and Fung, A. K. (1990b). *Microwave Remote Sensing Active and Passive*, volume I. Artech House, Inc.

Ulaby, F. T., Moore, R. K., and Fung, A. K. (1990c). *Microwave Remote Sensing Active and Passive*, volume II. Artech House, Inc.

Uppala, S., Broad, A., Delécluse, P., Köchy, M., Strahlendorff, M., Doherty, M., Schulz, J., Simmons, A., Kattenberg, A., Noyes, S., Fuchs, T., Jol, A., and Ehrhard, M. (2011). GMES Climate Service: Towards a European knowledge base in support of Mitigation and Adaptation. European Commission Enterprise and Industry Directorate-General. Draft Document DG ENTR/H.4/CC.

Urlichich, Y., Subbotin, V., Stupak, G., Dvorkin, V., Povalyaev, A., Karutin, S., and Bakitko, R. (2011). GLONASS Modernization. *GPS World*, 22(11).

Voronovich, A. G. (1985). Small Slope Approximation in Wave Scattering by Rough Surface. *Journal of Experimental and Theoretical Physics*, 62(1):65–70.

Voronovich, A. G. and Zavorotny, V. U. (2000). The Effect of Steep Sea-Waves on Polarization Ratio at Low Grazing Angles. *IEEE Transactions on Geoscience and Remote Sensing*, 38(1):366–373.

Wakabayashi, H. and Sakai, S. (2011). Sea ice area detection in the sea of Okhotsk using PALSAR polarimetric data. In *3rd International Asia-Pacific Conference on Conference on Synthetic Aperture Radar (APSAR)*, pages 1–4, Seoul, South Korea.

Wiehl, M., Legrésy, B., and Dietrich, R. (2003). Potential of reflected GNSS signals for ice sheet remote sensing. *Progress In Electromagnetics Research*, 40:177–205.

WMO (1989). World Meteorological Organization SEA-ICE NOMENCLATURE. WMO - No. 259.

Woodward, P. M. (1953). *Probability and Information Theory With Applications To Radar*. Pergamon Press, London, United Kingdom.

Yu, Y. and Rothrock, D. A. (1999). Thin ice thickness from satellite thermal imagery. *Journal of Geophysical Research*, 101(C11).

Zavorotny, V. U. and Voronovich, A. G. (2000). Scattering of GPS Signals from the Ocean with Wind Remote Sensing Application. *IEEE Transactions on Geoscience and Remote Sensing*, 38(2):951–964.

Zwally, H. J., Schutz, R., Abdalati, W., Abshire, J., Bentley, C., Brenner, A., Bufton, J., Dezio, J., Hancock, D., Harding, D., Herring, T., Minster, B., Quinn, K., Palm, S., Spinhirne, J., and Thomas, R. (2002). ICESAT's laser measurements of polar ice, atmosphere, ocean, and land. *Journal of Geodynamics*, 34:405–445.

Zwally, H. J., Schutz, R., Bentley, C., Bufton, J., Herring, T., Minster, J., Spinhirne, J., and Thomas, R. (2009). *GLAS/ICESat L2 Sea Ice Altimetry Data V031*. 2009, updated current year. 19 March 2005, 18 June 2005, 23 March 2006, 9 April 2007, 31 October 2007 and 6 April 2009. Boulder, Colorado USA: National Snow and Ice Data Center. Digital media.

Zwally, H. J., Yi, D., Kwok, R., and Zhao, Y. (2008). ICESat measurements of sea ice freeboard and estimates of sea ice thickness in the Weddell Sea. *Journal of Geophysical Research*, 113:3227–3246.